

# A structure-preserving parametric approximation for anisotropic geometric flows via an $\alpha$ -surface energy matrix

Weizhu Bao<sup>a</sup>, Yifei Li<sup>b</sup>, Wenjun Ying<sup>c</sup>, Yulin Zhang<sup>c</sup>

<sup>a</sup>*Department of Mathematics, National University of Singapore, Singapore, 119076*

<sup>b</sup>*Mathematisches Institut, Universität Tübingen, Auf der Morgenstelle 10, 72076, Tübingen, Germany*

<sup>c</sup>*School of Mathematical Sciences and Institute of Natural Sciences, Shanghai Jiao Tong University, Shanghai 200240, China*

---

## Abstract

We propose a structure-preserving parametric approximation for geometric flows with general anisotropic effects. By introducing a hyperparameter  $\alpha$ , we construct a unified surface energy matrix  $\hat{\mathbf{G}}_k^\alpha(\theta)$  that encompasses all existing formulations of surface energy matrices, and apply it to anisotropic curvature flow. We prove that  $\alpha = -1$  is the unique choice achieving optimal energy stability under the necessary and sufficient condition  $3\hat{\gamma}(\theta) \geq \hat{\gamma}(\theta - \pi)$ , while all other  $\alpha \neq -1$  require strictly stronger conditions. The framework extends naturally to general anisotropic geometric flows through a unified velocity discretization that ensures energy stability. Numerical experiments validate the theoretical optimality of  $\alpha = -1$  and demonstrate the effectiveness and robustness.

*Keywords:* geometric flows, parametric finite element method, anisotropy surface energy,  $\alpha$ -surface energy matrix, structure-preserving

---

## 1. Introduction

Curvature-driven evolution of curves and surfaces is fundamental to applications in image processing [1, 21, 53], materials science [30, 35, 38, 51, 56] and solid-state physics [41–43, 57, 61]. In crystalline materials, the underlying lattice structure naturally leads to the direction-dependent surface energy density. Such anisotropic effects are especially important when studying the evolution of crystal shapes or thin films, where the interfacial dynamics are strongly influenced by the material’s internal symmetry. Understanding and characterizing such anisotropic effects on the evolution of curves and surfaces is therefore crucial for both theoretical analysis and practical applications.

As illustrated in Fig 1, suppose  $\Gamma := \Gamma(t) \subset \mathbb{R}^2$  is an evolving closed two-dimensional (2D) curve associated with a given anisotropic surface energy density  $\hat{\gamma}(\theta) > 0$ , where  $\theta \in 2\pi\mathbb{T} := \mathbb{R}/2\pi\mathbb{Z}$  is the angle between the  $y$ -axis and the unit outward normal vector  $\mathbf{n} = \mathbf{n}(\theta) := (-\sin \theta, \cos \theta)^T$ . The evolution is driven by the weighted curvature  $\mu := \kappa_\gamma = [\hat{\gamma}(\theta) + \hat{\gamma}''(\theta)] \kappa$  given by [55], where  $\kappa$  is the classical curvature. This weighted curvature can also be viewed as the first variation of the total free energy  $W(\Gamma)$  defined by

$$W(\Gamma) := \int_{\Gamma} \hat{\gamma}(\theta) ds, \quad (1.1)$$

that is,

$$\mu = \frac{\delta W(\Gamma)}{\delta \Gamma} = \lim_{\varepsilon \rightarrow 0} \frac{W(\Gamma^\varepsilon) - W(\Gamma)}{\varepsilon}, \quad (1.2)$$

where  $\Gamma^\varepsilon$  is a small perturbation of  $\Gamma$ . When there is no anisotropic effect, i.e.  $\hat{\gamma}(\theta) \equiv \text{const}$ ,  $\mu$  reduces to  $\mu = \kappa$ .

---

*Email addresses:* matbaowz@nus.edu.sg (Weizhu Bao), yifei.li@mf.uni-tuebingen.de (Yifei Li), wying@sjtu.edu.cn (Wenjun Ying), yulin.zhang@sjtu.edu.cn (Yulin Zhang)

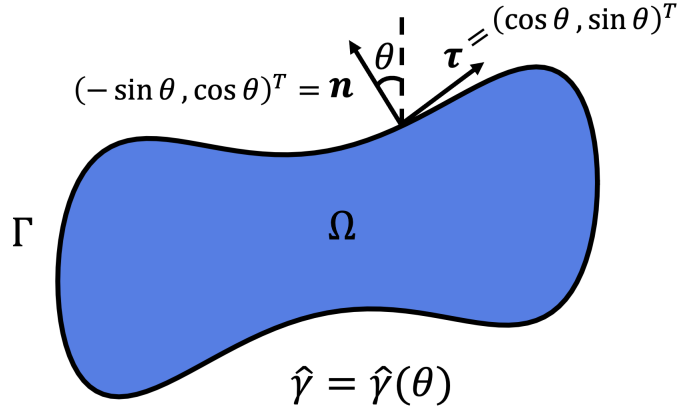


Figure 1: An illustration of an evolving closed curve with an anisotropic surface energy density  $\hat{\gamma}(\theta)$ . Here,  $\theta$  denotes the angle between the  $y$ -axis and the unit outward normal vector  $\mathbf{n} = \mathbf{n}(\theta) := (-\sin \theta, \cos \theta)^T$ . The unit tangent vector is  $\boldsymbol{\tau} = \boldsymbol{\tau}(\theta) := (\cos \theta, \sin \theta)^T$ .

Consider the anisotropic geometric evolution of closed curves in  $\mathbb{R}^2$  with normal velocity  $V_n$ . Several well-known anisotropic geometric flows, including the anisotropic curvature flow, area-conserved anisotropic curvature flow, and anisotropic surface diffusion, are given by:

$$V_n = \begin{cases} -\mu, & \text{anisotropic curvature flow,} \\ -\mu + \lambda, & \text{area-conserved anisotropic curvature flow,} \\ \partial_{ss}\mu, & \text{anisotropic surface diffusion,} \end{cases} \quad (1.3)$$

where  $\lambda := \int_{\Gamma} \mu ds / |\Gamma|$  is the Lagrange multiplier ensuring that the area of the region enclosed by  $\Gamma$  is conserved. The anisotropic geometric flows are related to gradient flows of anisotropic energy functionals such as  $W(\Gamma)$ , and therefore typically exhibit geometric properties such as energy dissipation and area conservation. Given the wide and profound applications of anisotropic geometric flows, developing a systematic framework of structure-preserving numerical schemes becomes particularly important.

Various numerical methods for isotropic curvature-driven problems have been conducted in the past few decades. For example, the level-set method [20, 48, 49], the phase-field method [19, 26], the marker particle method [25, 58], the finite element method [22, 23], the evolving surface finite element method (ESFEM) [39, 44, 45], and the parametric finite element method (PFEM) [9, 12, 27, 28, 46]. Among these approaches, the energy-stable PFEM (ES-PFEM) proposed by Barrett, Garcke, and Nürnberg [12, 15], commonly referred to as the BGN method, has gained significant attention owing to its unconditional energy stability and favorable mesh quality. The BGN method was successfully applied to a wide variety of isotropic curvature-driven problems, including the mean curvature flow [15], the surface diffusion [11], the multiphase flow [36, 37], the Stefan problem [34], the Mullins-Sekerka problem [16], and the evolution of open curves in solid-state dewetting [8, 63], consistently demonstrating robust computational performance. A key factor behind the success of BGN-type methods is, instead of approximating the curvature  $\kappa$  itself, they work with the *curvature vector*  $\kappa \mathbf{n}$  through the geometric identity

$$\kappa \mathbf{n} = -\partial_{ss} \mathbf{X} = -\partial_s \left( \mathbf{I}_d \partial_s \mathbf{X} \right), \quad (1.4)$$

here  $\mathbf{I}_d$  is the  $d$ -dimensional identity matrix. This approach provides a natural framework for achieving energy stability in isotropic curvature-driven problems. For more detailed discussions of the BGN-type methods, we refer the reader to the comprehensive review [18] by Barrett et al.

There have been numerous attempts to extend the ES-PFEM for isotropic geometric flows to the anisotropic setting. A common feature of these approaches is introducing a suitable surface energy matrix in place of  $\mathbf{I}_d$  in (1.4), yielding an analogous identity for the weighted curvature vector  $\mu \mathbf{n}$ . Barrett et al. first

achieved this for Riemannian-like surface energies  $\hat{\gamma}(\theta) = (\mathbf{n}(\theta) \cdot G\mathbf{n}(\theta))^{1/2}$  using the matrix  $\frac{1}{\hat{\gamma}(\theta)} \det(G) G^{-1}$  [14, 17]. In [46], Li and Bao constructed a surface energy matrix  $\hat{\mathbf{G}}(\theta) = \hat{\gamma}(\theta)I_2 - \mathbf{n}(\theta)\boldsymbol{\xi}(\theta)^T + \boldsymbol{\xi}(\theta)\mathbf{n}(\theta)^T$  based on the Cahn-Hoffman  $\boldsymbol{\xi}$ -vector, achieving the first extension to general surface energies, though with restrictive conditions on  $\hat{\gamma}(\theta)$ . In [3], Bao, Jiang, and Li introduced a stabilizing function  $k(\theta)$  and a symmetric surface energy matrix  $\hat{\mathbf{Z}}_k(\theta) = \hat{\gamma}(\theta)I_2 - \mathbf{n}\boldsymbol{\xi}^T - \boldsymbol{\xi}\mathbf{n}^T + k(\theta)\mathbf{n}\mathbf{n}^T$ , proving unconditional energy stability under the symmetry condition  $\hat{\gamma}(\theta) = \hat{\gamma}(\theta - \pi)$ . Through refined analysis [6, 47], this condition was later relaxed to  $3\hat{\gamma}(\theta) \geq \hat{\gamma}(\theta - \pi)$ . Similar stabilization techniques were also applied to  $\hat{\mathbf{G}}(\theta)$ , significantly improving its original stability conditions [4, 62].

The above studies reveal that different formulations of the surface energy matrix lead to different analyses. Moreover, the energy stability conditions for the resulting discrete schemes vary significantly and remain to be further refined. The main objective of this paper is to provide a unified analysis for the energy stability of SP-PFEMs that apply to all possible formulations of the surface energy matrix, through which we derive optimal energy stability conditions, and to conduct a systematic comparison of their computational performance. Our main contributions are as follows:

- **Unified surface energy matrix.** We introduce a hyperparameter  $\alpha \in \mathbb{R}$  and construct the unified  $\alpha$ -surface energy matrix

$$\hat{\mathbf{G}}_k^\alpha(\theta) := \hat{\gamma}(\theta)I_2 - \mathbf{n}\boldsymbol{\xi}^T + \alpha\boldsymbol{\xi}\mathbf{n}^T + k(\theta)\mathbf{n}\mathbf{n}^T, \quad (1.5)$$

which encompasses all existing formulations [3, 5, 47, 62] as special cases and exhausts all potential constructions (see Remark 2.3).

- **Optimal energy stability conditions.** We establish that the symmetric choice  $\alpha = -1$  is the only formulation achieving unconditional energy stability under the necessary and sufficient condition (see Remark 4.1).

$$3\hat{\gamma}(\theta) - \hat{\gamma}(\theta - \pi) \geq 0, \quad \forall \theta \in 2\pi\mathbb{T}. \quad (1.6)$$

All other formulations require the strictly stronger condition  $3\hat{\gamma}(\theta) - \hat{\gamma}(\theta - \pi) > 0$  unless additional constraints (e.g.,  $\hat{\gamma}'(\theta^*) = 0$ ) are imposed.

- **Unified velocity discretization.** We extend the SP-PFEM framework to the general anisotropic curvature-driven problems with normal velocity of the form

$$V_n = \mathfrak{F}(\mu), \quad (1.7)$$

where  $\mathfrak{F}$  is a mapping depending on the weighted curvature  $\mu$ . This formulation naturally encompasses all velocities in (1.3) and yields a unified discretization framework that ensures energy stability.

In addition, we conduct extensive numerical experiments to demonstrate the computational efficiency of the proposed method and investigate the effect of the parameter  $\alpha$ . The results demonstrate that the method effectively captures anisotropic curve evolution with robustness across different values of  $\alpha$ . Moreover, the experiments reveal several interesting phenomena in anisotropic geometric flows.

The structure of this paper is as follows: In section 2, we introduce a hyperparameter  $\alpha$  to establish a unified construction for all possible surface energy matrices and derive a conservative variational formulation for the anisotropic curvature flow. A full discretization by SP-PFEM is proposed in section 3. Concurrently, we state the structure-preserving property of the method. Section 4 offers a proof of the energy stability of SP-PFEM. Extensions to other anisotropic curvature-driven problems are discussed in section 5. We report extensive numerical experiments in section 6 to validate the accuracy, efficiency, structure-preserving property and robustness of the proposed SP-PFEM. Finally, we conclude the paper in section 7.

## 2. Anisotropic curvature flow and its variational formulation

### 2.1. The geometric PDE

Suppose the evolving curve  $\Gamma(t)$  is parameterized as  $\Gamma(t) : \mathbf{X}(s, t) = (x(s, t), y(s, t))^T \in \mathbb{R}^2$ , where  $s$  is the time-dependent arc-length parameter. Then the geometric evolution equation of the anisotropic curvature

flow in (1.3) can be described as follows:

$$\partial_t \mathbf{X} = -\mu \mathbf{n}, \quad 0 < s < L(t), \quad 0 \leq t \leq T, \quad (2.1a)$$

$$\mu = [\hat{\gamma}(\theta) + \hat{\gamma}''(\theta)] \kappa. \quad (2.1b)$$

Here,  $L(t) = |\Gamma(t)|$  denotes the length of  $\Gamma(t)$ ,  $T$  represents the maximum existing time.

It is noted that during the curve evolution, the velocity component in the tangential direction only affects the parameterization of the curve, without altering its geometric shape. Consequently, it suffices to prescribe the velocity vector  $V_n = \mathbf{n} \cdot \partial_t \mathbf{X}$  in the normal direction. Building on this observation, by allowing tangential motion, an equivalent formulation of the anisotropic curvature flow to that in (2.1) can be stated as the following geometric PDE:

$$\mathbf{n} \cdot \partial_t \mathbf{X} = -\mu, \quad 0 < s < L(t) \quad 0 \leq t \leq T, \quad (2.2a)$$

$$\mu = [\hat{\gamma}(\theta) + \hat{\gamma}''(\theta)] \kappa. \quad (2.2b)$$

*A unified  $\alpha$ -surface energy matrix*

To derive a conservative formulation for the anisotropic curvature flow (2.2), the following unified  $\alpha$ -surface energy matrix is introduced:

$$\hat{\mathbf{G}}_k^\alpha(\theta) := \hat{\gamma}(\theta) I_2 - \mathbf{n}(\theta) \boldsymbol{\xi}(\theta)^T + \alpha \boldsymbol{\xi}(\theta) \mathbf{n}(\theta)^T + k(\theta) \mathbf{n}(\theta) \mathbf{n}(\theta)^T, \quad (2.3)$$

with  $\boldsymbol{\xi}(\theta) = \hat{\gamma}(\theta) \mathbf{n}(\theta) - \hat{\gamma}'(\theta) \boldsymbol{\tau}(\theta)$  being the Cahn-Hoffman  $\boldsymbol{\xi}$ -vector,  $\alpha \in \mathbb{R}$  and  $k: 2\pi\mathbb{T} \rightarrow \mathbb{R}$  is a pre-determined stabilizing function.

**Lemma 2.1.** *For the weighted curvature  $\mu$  defined in (1.2), the following geometric identity holds:*

$$\mu \mathbf{n} + \partial_s \left( \hat{\mathbf{G}}_k^\alpha(\theta) \partial_s \mathbf{X} \right) = \mathbf{0}, \quad \forall \alpha \in \mathbb{R}. \quad (2.4)$$

*Proof.* From [40] or [62, Theorem 2.1], it is known that

$$\mu \mathbf{n} = -\partial_s \left( \hat{\gamma}(\theta) \partial_s \mathbf{X} + \hat{\gamma}'(\theta) \mathbf{n} \right). \quad (2.5)$$

Thus it remains to prove that

$$\hat{\mathbf{G}}_k^\alpha(\theta) \partial_s \mathbf{X} = \hat{\gamma}(\theta) \partial_s \mathbf{X} + \hat{\gamma}'(\theta) \mathbf{n}. \quad (2.6)$$

Noting that  $\mathbf{n} = (-\sin \theta, \cos \theta)^T$ ,  $\boldsymbol{\tau} = (\cos \theta, \sin \theta)^T$ , we have

$$\hat{\mathbf{G}}_k^\alpha(\theta) = \hat{\gamma}(\theta) I_2 + \hat{\gamma}'(\theta) (\mathbf{n} \boldsymbol{\tau}^T - \alpha \boldsymbol{\tau} \mathbf{n}^T) + (k(\theta) + (\alpha - 1) \hat{\gamma}(\theta)) \mathbf{n} \mathbf{n}^T. \quad (2.7)$$

Combining (2.7) with the facts  $\partial_s \mathbf{X} = \boldsymbol{\tau}$  and  $\mathbf{n}^T \partial_s \mathbf{X} \equiv 0$  yields

$$\begin{aligned} \hat{\mathbf{G}}_k^\alpha(\theta) \partial_s \mathbf{X} &= \hat{\gamma}(\theta) \partial_s \mathbf{X} + \hat{\gamma}'(\theta) \mathbf{n} + (-\alpha \hat{\gamma}'(\theta) \boldsymbol{\tau} \mathbf{n}^T + (k(\theta) + (\alpha - 1) \hat{\gamma}(\theta)) \mathbf{n} \mathbf{n}^T) \partial_s \mathbf{X} \\ &= \hat{\gamma}(\theta) \partial_s \mathbf{X} + \hat{\gamma}'(\theta) \mathbf{n}. \end{aligned} \quad (2.8)$$

This proves the lemma. □

Applying the identity (2.4), a *strong formulation* for the geometric PDE (2.2a)–(2.2b) is expressed as follows:

$$\mathbf{n} \cdot \partial_t \mathbf{X} + \mu = 0, \quad 0 < s < L(t), \quad \forall 0 \leq t \leq T, \quad (2.9a)$$

$$\mu \mathbf{n} + \partial_s \left( \hat{\mathbf{G}}_k^\alpha(\theta) \partial_s \mathbf{X} \right) = \mathbf{0}, \quad (2.9b)$$

where  $L(t)$  is the length of the evolving curve  $\Gamma(t)$ .

**Remark 2.1.** When  $\gamma(\theta) \equiv 1$ , the weighted curvature  $\mu$  reduces to the classical curvature  $\kappa$ , and by taking  $k(\theta) \equiv 1 - \alpha$ , we have the surface energy matrix  $\hat{\mathbf{G}}_k^\alpha(\theta) \equiv I_2$ . Thus (2.9) will reduce to the standard formulation by BGN method for mean curvature flow [12].

**Remark 2.2.** By selecting different parameter  $\alpha$ , the strong form (2.9) will generate different formulations for the weighted curvature  $\mu$ . For example, when  $\alpha = -1$ , it offers the symmetrized formulations in [3, 47]; by setting  $\alpha = 0, k(\theta) \equiv 0$ , we will obtain the formulation proposed in [13]; and it will lead to the formulations in [4, 46, 62] by choosing  $\alpha = 1$ .

**Remark 2.3.** For any surface energy matrix  $\hat{\mathbf{G}}(\theta)$  satisfying  $\mu \mathbf{n} = -\partial_s (\hat{\mathbf{G}}(\theta) \partial_s \mathbf{X})$ , it can be obtained by  $\hat{\mathbf{G}}_k^\alpha(\theta)$  in (2.3). To see this, consider  $K(\boldsymbol{\tau}) := \{\mathbf{A} \in \mathbb{R}^{2 \times 2} \mid \mathbf{A} \boldsymbol{\tau} = \mathbf{0}\}$  with  $\dim K(\boldsymbol{\tau}) = 2$  and  $\boldsymbol{\xi} \mathbf{n}^T, \mathbf{n} \mathbf{n}^T \in K(\boldsymbol{\tau})$ . For the anisotropic case, as  $\boldsymbol{\xi} \nparallel \mathbf{n}$ ,  $K(\boldsymbol{\tau}) = \{\alpha \boldsymbol{\xi} \mathbf{n}^T + k \mathbf{n} \mathbf{n}^T \mid \alpha, k \in \mathbb{R}\}$ . We know that  $\hat{\mathbf{G}}(\theta) - \hat{\mathbf{G}}_0^0(\theta) \in K(\boldsymbol{\tau})$  since  $\mu \mathbf{n} = -\partial_s (\hat{\mathbf{G}}(\theta) \partial_s \mathbf{X}) = -\partial_s (\hat{\mathbf{G}}_0^0(\theta) \partial_s \mathbf{X})$ . Therefore, we can deduce that  $\hat{\mathbf{G}}(\theta) \in \hat{\mathbf{G}}_0^0(\theta) + K(\boldsymbol{\tau}) = \{\hat{\mathbf{G}}_k^\alpha(\theta) \mid \alpha, k \in \mathbb{R}\}$ . This shows that all possible surface energy matrix can be expressed in the form of (2.3).

## 2.2. Variational formulation

To obtain a variational formulation based on the strong form (2.9), we suppose the evolving  $\Gamma(t)$  is parametrized by a time-independent parameter  $\rho$  over a fixed domain  $\mathbb{I} := [0, 1]$ , i.e.

$$\Gamma(t): \mathbf{X}(\rho, t) = (x(\rho, t), y(\rho, t))^T, \quad \forall \rho \in \mathbb{I}, t \in [0, T]. \quad (2.10)$$

Thus the arc-length parameterization can be computed as  $s(\rho, t) = \int_0^\rho |\partial_r \mathbf{X}(r, t)| dr$ . In this paper, we make no distinction between  $\mathbf{X}(s, t)$  and  $\mathbf{X}(\rho, t)$  and assume the parameterization by  $\rho$  is always regular, i.e.  $\frac{1}{C} \leq |\partial_r s(\rho, t)| \leq C, \forall \rho \in \mathbb{I}$  for a constant  $C > 1$ .

For an evolving curve  $\Gamma(t)$ , the  $L^2$ -space with respect to  $\Gamma(t)$  is defined as follows:

$$L^2(\mathbb{I}) := \left\{ u: \mathbb{I} \rightarrow \mathbb{R} \mid \int_{\Gamma(t)} |u(s)|^2 ds = \int_{\mathbb{I}} |u(s(\rho, t))|^2 \partial_\rho s d\rho < +\infty \right\}, \quad (2.11)$$

equipped with the inner product

$$\left( u, v \right)_{\Gamma(t)} := \int_{\Gamma(t)} u(s)v(s) ds = \int_{\mathbb{I}} u(s(\rho, t))v(s(\rho, t)) \partial_\rho s d\rho, \quad \forall u, v \in L^2(\mathbb{I}). \quad (2.12)$$

And the corresponding Sobolev spaces are given as

$$H^1(\mathbb{I}) := \{u \in L^2(\mathbb{I}) \mid \partial_\rho u \in L^2(\mathbb{I})\}, \quad H_p^1(\mathbb{I}) := \{u \in H^1(\mathbb{I}) \mid u(0) = u(1)\}. \quad (2.13a)$$

Multiplying test functions  $\varphi \in H_p^1(\mathbb{I})$  to (2.9a) and  $\boldsymbol{\omega} = (\omega_1, \omega_2)^T \in [H_p^1(\mathbb{I})]^2$  to (2.9b), respectively. Then integrating over  $\Gamma(t)$  and applying integration by parts, we obtain the *variational formulation* for the strong form (2.9) as follows: Suppose the initial closed curve  $\Gamma(0) := \mathbf{X}(\cdot, 0) = (x(\cdot, 0), y(\cdot, 0))^T \in [H_p^1(\mathbb{I})]^2$  and the initial weighted curvature  $\mu(\cdot, 0) := \mu_0(\cdot) \in H_p^1(\mathbb{I})$ , for any  $t > 0$ , find the solution  $(\mathbf{X}(\cdot, t) = (x(\cdot, t), y(\cdot, t))^T, \mu(\cdot, t)) \in [H_p^1(\mathbb{I})]^2 \times H_p^1(\mathbb{I})$  such that

$$\left( \mathbf{n} \cdot \partial_t \mathbf{X}, \varphi \right)_{\Gamma(t)} + \left( \mu, \varphi \right)_{\Gamma(t)} = 0, \quad \forall \varphi \in H_p^1(\mathbb{I}), \quad (2.14a)$$

$$\left( \mu \mathbf{n}, \boldsymbol{\omega} \right)_{\Gamma(t)} - \left( \hat{\mathbf{G}}_k^\alpha(\theta) \partial_s \mathbf{X}, \partial_s \boldsymbol{\omega} \right)_{\Gamma(t)} = 0, \quad \forall \boldsymbol{\omega} \in [H_p^1(\mathbb{I})]^2. \quad (2.14b)$$

### 2.3. Properties of the variational formulation

Denote  $A(t)$  as the total area enclosed by the evolving curve  $\Gamma(t)$ , and  $W(t)$  as the total interfacial energy, which are formally defined as

$$A(t) := \int_{\Gamma(t)} y(s, t) \partial_s x(s, t) \, ds, \quad W(t) := \int_{\Gamma(t)} \hat{\gamma}(\theta) \, ds. \quad (2.15)$$

To derive the area decay rate and the energy dissipation rate, we need the time derivative of the inclination angle  $\partial_t \theta$  as well as the transport lemma.

**Lemma 2.2.** *For the time derivative of the inclination angle  $\theta$ , the following geometric identity holds:*

$$\partial_t \theta = \partial_s (\partial_t \mathbf{X}) \cdot \mathbf{n}. \quad (2.16)$$

*Proof.* Firstly, consider the time derivative of  $|\partial_\rho \mathbf{X}| = \sqrt{(\partial_\rho x)^2 + (\partial_\rho y)^2}$ . Then

$$\partial_t |\partial_\rho \mathbf{X}| = \frac{\partial_\rho x \partial_t (\partial_\rho x) + \partial_\rho y \partial_t (\partial_\rho y)}{\sqrt{(\partial_\rho x)^2 + (\partial_\rho y)^2}} = \frac{\partial_\rho \mathbf{X}}{|\partial_\rho \mathbf{X}|} \cdot \frac{\partial_\rho (\partial_t \mathbf{X})}{|\partial_\rho \mathbf{X}|} |\partial_\rho \mathbf{X}| = \partial_s \mathbf{X} \cdot \partial_s (\partial_t \mathbf{X}) |\partial_\rho \mathbf{X}|. \quad (2.17)$$

Therefore, by (2.17),

$$\begin{aligned} \partial_s (\partial_t \mathbf{X}) &= \frac{1}{|\partial_\rho \mathbf{X}|} \partial_\rho (\partial_t \mathbf{X}) = \frac{1}{|\partial_\rho \mathbf{X}|} \partial_t (|\partial_\rho \mathbf{X}| (\cos \theta, \sin \theta)^T) \\ &= \partial_s \mathbf{X} \cdot \partial_s (\partial_t \mathbf{X}) (\cos \theta, \sin \theta)^T + (-\sin \theta, \cos \theta)^T \partial_t \theta. \end{aligned} \quad (2.18)$$

Combining with the fact that  $\mathbf{n} = (-\sin \theta, \cos \theta)^T$  gives the desired result.  $\square$

**Lemma 2.3** (Transport lemma, [62]). *Suppose  $\Gamma(t)$  is a two-dimensional piecewise  $C^1$  curve parameterized by  $\mathbf{X}(\rho, t)$ , function  $f : \Gamma(t) \times \mathbb{R}^+ \rightarrow \mathbb{R}$  is differentiable. Then*

$$\frac{d}{dt} \int_{\Gamma(t)} f \, ds = \int_{\Gamma(t)} \partial_t f + f \partial_s (\partial_t \mathbf{X}) \cdot \partial_s \mathbf{X} \, ds. \quad (2.19)$$

**Proposition 2.1** (Area decay rate and energy dissipation). *Let  $(\mathbf{X}(\cdot, t), \mu(\cdot, t))$  be the solution to the variational formulation (2.14). Then the total area  $A(t)$  satisfies the following decay rate and the total interfacial energy  $W(t)$  is dissipative, i.e.,*

$$\frac{dA}{dt} = -(\mu, 1)_{\Gamma(t)}, \quad W(t) \leq W(t') \leq W(0), \quad \forall t \geq t' \geq 0. \quad (2.20)$$

*Proof.* Denote  $\Omega(t)$  the region enclosed by  $\Gamma(t)$ . Applying the Reynolds' transport theorem [52] and taking  $\varphi = 1$  in (2.14a),

$$\frac{d}{dt} A(t) = \frac{d}{dt} \int_{\Omega(t)} dx \, dy = \int_{\Gamma(t)} \mathbf{n} \cdot \partial_t \mathbf{X} \, ds = (\mathbf{n} \cdot \partial_t \mathbf{X}, 1)_{\Gamma(t)} = -(\mu, 1)_{\Gamma(t)}. \quad (2.21)$$

For the energy dissipation, differentiating  $W(t)$  with respect to  $t$  by Lemma 2.3,

$$\frac{d}{dt} W(t) = \int_{\Gamma(t)} \hat{\gamma}'(\theta) \partial_t \theta + \hat{\gamma}(\theta) \partial_s (\partial_t \mathbf{X}) \cdot \partial_s \mathbf{X} \, ds. \quad (2.22)$$

Combining with the geometric identity (2.16) of  $\theta$ , we have

$$\frac{d}{dt} W(t) = \int_{\Gamma(t)} [\hat{\gamma}(\theta) \partial_s \mathbf{X} + \hat{\gamma}'(\theta) \mathbf{n}] \cdot \partial_s (\partial_t \mathbf{X}) \, ds = \int_{\Gamma(t)} \hat{\mathbf{G}}_k^\alpha(\theta) \partial_s \mathbf{X} \cdot \partial_s (\partial_t \mathbf{X}) \, ds. \quad (2.23)$$

By setting  $\varphi = \mu$  in (2.14a) and  $\boldsymbol{\omega} = \partial_t \mathbf{X}$  in (2.14b), and considering (2.23), then

$$\frac{d}{dt} W(t) = \left( \hat{\mathbf{G}}_k^\alpha(\theta) \partial_s \mathbf{X}, \partial_s (\partial_t \mathbf{X}) \right)_{\Gamma(t)} = (\mu \mathbf{n}, \partial_t \mathbf{X})_{\Gamma(t)} = -(\mu, \mu)_{\Gamma(t)} \leq 0. \quad (2.24)$$

$\square$

### 3. A structure-preserving parametric finite element approximation

In this section, a parametric finite element full discretization is proposed based on the variational form (2.14), which preserves both the area decay rate and the energy dissipation.

Let  $N > 2$  be a positive integer and define the mesh size as  $h = 1/N$ . Consider a uniform partition of the interval as  $\mathbb{I} = [0, 1] := \cup_{j=1}^N I_j$  with  $I_j = [\rho_{j-1}, \rho_j]$ ,  $\rho_j := jh$  for  $j = 0, 1, \dots, N$ . The piecewise linear finite element spaces are defined as

$$\mathbb{K}^h := \{u^h \in C(\mathbb{I}) \mid u^h|_{I_j} \in \mathcal{P}^1(I_j), \forall j = 1, 2, \dots, N\} \subseteq H^1(\mathbb{I}), \quad (3.1a)$$

$$\mathbb{K}_p^h := \{u^h \in \mathbb{K}^h \mid u^h(0) = u^h(1)\} \subseteq H_p^1(\mathbb{I}), \quad (3.1b)$$

where  $\mathcal{P}^1(I_j)$  represents the space of all polynomials on the interval  $I_j$  with degree at most 1. Additionally, we define  $0 = t_0 < t_1 < \dots < t_M = T$  be a uniform partition of  $[0, T]$  with time steps  $t_m = m\tau$ ,  $\tau := T/M$ .

Let  $\Gamma^m := \mathbf{X}^m(\cdot) \in [\mathbb{K}_p^h]^2$  be an approximation of  $\Gamma(t_m) = \mathbf{X}(\cdot, t_m = m\tau)$ , satisfies the following non-degeneracy condition:

$$\min_{1 \leq j \leq N} |\mathbf{h}_j^m| > 0, \quad \forall m = 0, 1, \dots, M, \quad (3.2)$$

where  $\mathbf{h}_j^m := \mathbf{X}^m(\rho_j) - \mathbf{X}^m(\rho_{j-1})$  and  $u(\rho_j^\pm) = \lim_{\rho \rightarrow \rho_j^\pm} u(\rho)$ . Similarly,  $\mu^m \in \mathbb{K}_p^h$  denotes an approximation of  $\mu(\cdot, t_m)$ .

The mass-lumped inner product for  $u, v \in \mathbb{K}_p^h$  is defined as follows:

$$(u, v)_{\Gamma^m}^h := \sum_{j=1}^N \frac{|\mathbf{h}_j^m|}{2} (u(\rho_j^-)v(\rho_j^-) + u(\rho_{j-1}^+)v(\rho_{j-1}^+)). \quad (3.3)$$

And the discretized derivative  $\partial_s$  on  $\Gamma^m$  is defined as

$$\partial_s f|_{I_j} := \frac{f(\rho_j) - f(\rho_{j-1})}{|\mathbf{h}_j^m|}, \quad \forall j = 1, 2, \dots, N. \quad (3.4)$$

The above definitions can be directly extended to vector-valued functions.

Discrete geometric quantities such as the unit tangential vector  $\boldsymbol{\tau}^m$ , the unit normal vector  $\mathbf{n}^m$  and the inclination angle  $\theta^m$  of the polygonal curve  $\Gamma^m$  can be computed as

$$\boldsymbol{\tau}^m|_{I_j} = \frac{\mathbf{h}_j^m}{|\mathbf{h}_j^m|} := \boldsymbol{\tau}_j^m, \quad \mathbf{n}^m|_{I_j} = -\frac{(\mathbf{h}_j^m)^\perp}{|\mathbf{h}_j^m|} := \mathbf{n}_j^m, \quad (3.5)$$

and

$$\theta^m|_{I_j} = \theta_j^m, \quad \text{where } \theta_j^m \text{ satisfying } (\cos \theta_j^m, \sin \theta_j^m)^T = \boldsymbol{\tau}_j^m. \quad (3.6)$$

Now we are ready to present a structure-preserving parametric finite element approximation for the anisotropic curvature flow (2.2a)–(2.2b):

Suppose  $\Gamma^0 \in [\mathbb{K}_p^h]^2$  be the initial approximation given by  $\mathbf{X}^0(\rho_j) = \mathbf{X}(\rho_j, 0)$ ,  $j = 1, 2, \dots, N$ . Find the solution  $(\mathbf{X}^{m+1}(\cdot) = (x^m(\cdot), y^m(\cdot))^T, \mu^{m+1}(\cdot)) \in [\mathbb{K}_p^h]^2 \times \mathbb{K}_p^h$ ,  $m = 0, 1, \dots, M-1$ , such that

$$\left( \mathbf{n}^{m+\frac{1}{2}} \cdot \frac{\mathbf{X}^{m+1} - \mathbf{X}^m}{\tau}, \varphi^h \right)_{\Gamma^m}^h + \left( \mu^{m+1}, \varphi^h \right)_{\Gamma^m}^h = 0, \quad \forall \varphi^h \in \mathbb{K}_p^h, \quad (3.7a)$$

$$\left( \mu^{m+1} \mathbf{n}^{m+\frac{1}{2}}, \boldsymbol{\omega}^h \right)_{\Gamma^m}^h - \left( \hat{\mathbf{G}}_k^\alpha(\theta^m) \partial_s \mathbf{X}^{m+1}, \partial_s \boldsymbol{\omega}^h \right)_{\Gamma^m}^h = 0, \quad \forall \boldsymbol{\omega}^h \in [\mathbb{K}_p^h]^2, \quad (3.7b)$$

where

$$\mathbf{n}^{m+\frac{1}{2}} := -\frac{1}{2} (\partial_s \mathbf{X}^m + \partial_s \mathbf{X}^{m+1})^\perp = -\frac{1}{2|\partial_\rho \mathbf{X}^m|} (\partial_\rho \mathbf{X}^m + \partial_\rho \mathbf{X}^{m+1})^\perp. \quad (3.8)$$

**Remark 3.1.** The choice of  $\mathbf{n}^{m+\frac{1}{2}}$  is motivated by the area-preserving PFEM proposed by Bao and Zhao for surface diffusion [7]. It rigorously characterizes the area difference of a evolving polygonal curve between two discrete time levels, making it crucial for maintaining the area decay rate.

### 3.1. Area decay rate preserving and energy dissipation properties of the SP-PFEM

Let  $A^m$  be the area enclosed by the polygonal curve  $\Gamma^m$ , and  $W^m$  be the total interfacial energy, which are given by

$$A^m := \frac{1}{2} \sum_{j=1}^N (x^m(\rho_j) - x^m(\rho_{j-1})) (y^m(\rho_j) + y^m(\rho_{j-1})), \quad W^m := \sum_{j=1}^N \hat{\gamma}(\theta_j^m) |\mathbf{h}_j^m|. \quad (3.9)$$

Our main result is stated as follows:

**Theorem 3.1** (structure-preserving). *The SP-PFEM (3.7) is area decay rate preserving, i.e.,*

$$\frac{A^{m+1} - A^m}{\tau} = - \left( \mu^{m+1}, 1 \right)_{\Gamma^m}^h, \quad \forall 0 \leq m \leq M-1. \quad (3.10)$$

Moreover, if  $\alpha = -1$  and  $\hat{\gamma}(\theta) \in C^2(2\pi\mathbb{T})$  satisfies

$$3\hat{\gamma}(\theta) - \hat{\gamma}(\theta - \pi) \geq 0, \quad \forall \theta \in 2\pi\mathbb{T}. \quad (3.11)$$

Then the SP-PFEM (3.7) is unconditionally energy stable with sufficiently large  $k(\theta)$ , i.e.,

$$W^{m+1} \leq W^m \leq \dots \leq W^0, \quad \forall 0 \leq m \leq M-1. \quad (3.12)$$

Otherwise, for  $\alpha \neq -1$ , the energy stability condition (3.11) needs to be strengthened to

$$3\hat{\gamma}(\theta) - \hat{\gamma}(\theta - \pi) > 0, \quad \forall \theta \in 2\pi\mathbb{T}. \quad (3.13)$$

We only provide a proof for area decay rate preserving property here, and leave the energy dissipation part to the next section.

*Proof.* Similar to derivations of [7, Theorem 2.1], we have

$$A^{m+1} - A^m = \left( \mathbf{n}^{m+\frac{1}{2}} \cdot (\mathbf{X}^{m+1} - \mathbf{X}^m), 1 \right)_{\Gamma^m}^h. \quad (3.14)$$

Thus by taking  $\varphi^h \equiv 1$  in (3.7a), we obtain

$$A^{m+1} - A^m = -\tau \left( \mu^{m+1}, 1 \right)_{\Gamma^m}^h. \quad (3.15)$$

This establishes the area decay rate formula.  $\square$

## 4. Proof of the unconditional energy stability

### 4.1. Minimal stabilizing function and unconditional energy stability

To prove the unconditional energy dissipation property of the SP-PFEM (3.7), we first introduce a minimal stabilizing function  $k_{\min}^\alpha(\theta)$ , which is defined as

$$k_{\min}^\alpha(\theta) := k_0^\alpha(\theta) - (\alpha - 1)\hat{\gamma}(\theta), \quad \forall \theta \in 2\pi\mathbb{T}, \quad (4.1)$$

where  $k_0^\alpha(\theta)$  is given by

$$k_0^\alpha(\theta) := \inf \{ a \geq 0 \mid 4\hat{\gamma}(\theta)P_{\alpha,a}(\phi, \theta) \geq Q_\alpha^2(\phi, \theta), \forall \phi \in 2\pi\mathbb{T} \}. \quad (4.2)$$

Here,  $P_{\alpha,a}, Q_\alpha$  are two auxiliary functions defined as

$$P_{\alpha,a}(\phi, \theta) := \hat{\gamma}(\theta) + \frac{\alpha - 1}{2} \hat{\gamma}'(\theta) \sin 2\phi + a \sin^2 \phi, \quad (4.3a)$$

$$Q_\alpha(\phi, \theta) := \hat{\gamma}(\theta - \phi) + \hat{\gamma}(\theta) \cos \phi + \alpha \hat{\gamma}'(\theta) \sin \phi. \quad (4.3b)$$

**Assumption 4.1.** Suppose for a given  $\hat{\gamma}(\theta) \in C^2(2\pi\mathbb{T})$  and  $\alpha \in \mathbb{R}$ , the minimal stabilizing function  $k_{\min}^\alpha(\theta)$  exists, i.e.

$$k_{\min}^\alpha(\theta) < +\infty, \quad \forall \theta \in 2\pi\mathbb{T}. \quad (4.4)$$

The following local energy estimate is established under Assumption 4.1:

**Lemma 4.1** (local energy estimate). Assume that (4.4) holds true. For any  $\mathbf{p}, \mathbf{q} \in \mathbb{R}^2 \setminus \{\mathbf{0}\}$ , let  $\mathbf{p} = |\mathbf{p}|(\cos \varphi, \sin \varphi)^T$ ,  $\mathbf{q} = |\mathbf{q}|(\cos \theta, \sin \theta)^T$ . Then for sufficiently large  $k(\theta)$ ,

$$\frac{1}{|\mathbf{q}|} \left( \hat{\mathbf{G}}_k^\alpha(\theta) \mathbf{p} \right) \cdot (\mathbf{p} - \mathbf{q}) \geq \hat{\gamma}(\varphi) |\mathbf{p}| - \hat{\gamma}(\theta) |\mathbf{q}|. \quad (4.5)$$

*Proof.* Recall the definition (2.3) of  $\hat{\mathbf{G}}_k^\alpha(\theta)$ , then

$$\begin{aligned} \frac{1}{|\mathbf{q}|} \left( \hat{\mathbf{G}}_k^\alpha(\theta) \mathbf{p} \right) \cdot \mathbf{p} &= \frac{|\mathbf{p}|^2}{|\mathbf{q}|} \left( \hat{\mathbf{G}}_k^\alpha(\theta) \begin{pmatrix} \cos \varphi \\ \sin \varphi \end{pmatrix} \right) \cdot \begin{pmatrix} \cos \varphi \\ \sin \varphi \end{pmatrix} \\ &= \frac{|\mathbf{p}|^2}{|\mathbf{q}|} \left( \hat{\gamma}(\theta) + (\alpha - 1) \hat{\gamma}'(\theta) \sin(\theta - \varphi) \cos(\theta - \varphi) + (k(\theta) + (\alpha - 1) \hat{\gamma}(\theta)) \sin^2(\theta - \varphi) \right) \\ &= \frac{|\mathbf{p}|^2}{|\mathbf{q}|} \left( \hat{\gamma}(\theta) + \frac{\alpha - 1}{2} \hat{\gamma}'(\theta) \sin(2(\theta - \varphi)) + (k(\theta) + (\alpha - 1) \hat{\gamma}(\theta)) \sin^2(\theta - \varphi) \right) \\ &= \frac{|\mathbf{p}|^2}{|\mathbf{q}|} P_{\alpha, k + (\alpha - 1) \hat{\gamma}}(\theta - \varphi, \theta), \end{aligned} \quad (4.6)$$

and

$$\begin{aligned} \frac{1}{|\mathbf{q}|} \left( \hat{\mathbf{G}}_k^\alpha(\theta) \mathbf{p} \right) \cdot \mathbf{q} &= |\mathbf{p}| \left( \hat{\mathbf{G}}_k^\alpha(\theta) \begin{pmatrix} \cos \varphi \\ \sin \varphi \end{pmatrix} \right) \cdot \begin{pmatrix} \cos \theta \\ \sin \theta \end{pmatrix} \\ &= |\mathbf{p}| \left( \hat{\gamma}(\theta) \cos(\theta - \varphi) + \alpha \hat{\gamma}'(\theta) \sin(\theta - \varphi) \right) \\ &= |\mathbf{p}| (Q_\alpha(\theta - \varphi, \theta) - \hat{\gamma}(\varphi)). \end{aligned} \quad (4.7)$$

Suppose that (4.4) is satisfied. Then for sufficiently large  $k(\theta) \geq k_{\min}^\alpha(\theta)$ , we know  $k(\theta) + (\alpha - 1) \hat{\gamma}(\theta) \geq k_{\min}^\alpha(\theta) + (\alpha - 1) \hat{\gamma}(\theta) = k_0^\alpha(\theta)$ . Thus, from (4.2), we have

$$\begin{aligned} 4\hat{\gamma}(\theta) P_{\alpha, k + (\alpha - 1) \hat{\gamma}}(\theta - \varphi, \theta) &= 4\hat{\gamma}(\theta) P_{\alpha, k_0^\alpha}(\theta - \varphi, \theta) + 4\hat{\gamma}(\theta) (k(\theta) - k_{\min}^\alpha(\theta)) \sin^2(\theta - \varphi) \\ &\geq 4\hat{\gamma}(\theta) P_{\alpha, k_0^\alpha}(\theta - \varphi, \theta) \geq Q_\alpha^2(\theta - \varphi, \theta), \quad \forall \varphi \in 2\pi\mathbb{T}. \end{aligned} \quad (4.8)$$

Combining with the fact that  $\frac{1}{4c}x^2 - x \geq -c$ ,  $\forall x \in \mathbb{R}$ ,  $c > 0$  gives

$$\begin{aligned} \frac{1}{|\mathbf{q}|} \left( \hat{\mathbf{G}}_k^\alpha(\theta) \mathbf{p} \right) \cdot (\mathbf{p} - \mathbf{q}) &= \frac{|\mathbf{p}|^2}{|\mathbf{q}|} P_{\alpha, k + (\alpha - 1) \hat{\gamma}}(\theta - \varphi, \theta) - |\mathbf{p}| (Q_\alpha(\theta - \varphi, \theta) - \hat{\gamma}(\varphi)) \\ &\geq \hat{\gamma}(\varphi) |\mathbf{p}| + \left( \frac{1}{4\hat{\gamma}(\theta) |\mathbf{q}|} (|\mathbf{p}| Q_\alpha(\theta - \varphi, \theta))^2 - |\mathbf{p}| Q_\alpha(\theta - \varphi, \theta) \right) \\ &\geq \hat{\gamma}(\varphi) |\mathbf{p}| - \hat{\gamma}(\theta) |\mathbf{q}|, \end{aligned} \quad (4.9)$$

which is the desired result.  $\square$

**Remark 4.1.** Following the analysis in [4, 47, 62], taking  $\mathbf{p} = -\mathbf{q}$  (i.e.,  $\varphi = \theta - \pi$ ) in (4.5) yields the necessary condition  $3\hat{\gamma}(\theta) \geq \hat{\gamma}(\theta - \pi)$  for the local energy estimate. Comparing this with condition (3.11) for  $\alpha = -1$ , we conclude that (3.11) is both necessary and sufficient for the local energy estimate when  $\alpha = -1$ , and is therefore optimal.

**Remark 4.2.** For the isotropic case, i.e.  $\hat{\gamma}(\theta) \equiv 1$ , it is easy to see that  $k_0^\alpha(\theta) \equiv 0$  for any  $\alpha \in \mathbb{R}$ . This indicates that the minimal stabilizing function  $k_{\min}^\alpha(\theta) \equiv 1 - \alpha$ .

With the local energy estimate (4.5), the unconditional energy dissipation property of SP-PFEM (3.7) can be proven under Assumption 4.1:

*Proof.* Suppose  $k(\theta)$  is sufficiently large such that  $k(\theta) \geq k_{\min}^\alpha(\theta)$ .

Then for  $\forall 0 \leq m \leq M-1$ ,

$$\begin{aligned} \left( \hat{\mathbf{G}}_k^\alpha(\theta^m) \partial_s \mathbf{X}^{m+1}, \partial_s (\mathbf{X}^{m+1} - \mathbf{X}^m) \right)_{\Gamma^m}^h &= \sum_{j=1}^N \left[ |\mathbf{h}_j^m| \left( \hat{\mathbf{G}}_k^\alpha(\theta^m) \frac{\mathbf{h}_j^{m+1}}{|\mathbf{h}_j^m|} \right) \cdot \frac{\mathbf{h}_j^{m+1} - \mathbf{h}_j^m}{|\mathbf{h}_j^m|} \right] \\ &= \sum_{j=1}^N \left[ \frac{1}{|\mathbf{h}_j^m|} \left( \hat{\mathbf{G}}_k^\alpha(\theta^m) \mathbf{h}_j^{m+1} \right) \cdot (\mathbf{h}_j^{m+1} - \mathbf{h}_j^m) \right]. \end{aligned} \quad (4.10)$$

Applying the local energy estimate (4.5) by letting  $\mathbf{p} = \mathbf{h}_j^{m+1} = |\mathbf{h}_j^{m+1}|(\cos \theta_j^{m+1}, \sin \theta_j^{m+1})^T$ ,  $\mathbf{q} = \mathbf{h}_j^m = |\mathbf{h}_j^m|(\cos \theta_j^m, \sin \theta_j^m)^T$ ,

$$\begin{aligned} \left( \hat{\mathbf{G}}_k^\alpha(\theta^m) \partial_s \mathbf{X}^{m+1}, \partial_s (\mathbf{X}^{m+1} - \mathbf{X}^m) \right)_{\Gamma^m}^h &\geq \sum_{j=1}^N [\hat{\gamma}(\theta_j^{m+1}) |\mathbf{h}_j^{m+1}| - \hat{\gamma}(\theta_j^m) |\mathbf{h}_j^m|] \\ &= \sum_{j=1}^N \hat{\gamma}(\theta_j^{m+1}) |\mathbf{h}_j^{m+1}| - \sum_{j=1}^N \hat{\gamma}(\theta_j^m) |\mathbf{h}_j^m| \\ &= W^{m+1} - W^m. \end{aligned} \quad (4.11)$$

Therefore, by taking  $\varphi^h = \mu^{m+1}$  and  $\boldsymbol{\omega}^h = \mathbf{X}^{m+1} - \mathbf{X}^m$  in (3.7), we conclude that

$$\begin{aligned} W^{m+1} - W^m &\leq \left( \hat{\mathbf{G}}_k^\alpha(\theta^m) \partial_s \mathbf{X}^{m+1}, \partial_s (\mathbf{X}^{m+1} - \mathbf{X}^m) \right)_{\Gamma^m}^h \\ &= \left( \mu^{m+1} \mathbf{n}^{m+\frac{1}{2}}, \mathbf{X}^{m+1} - \mathbf{X}^m \right)_{\Gamma^m}^h = -\tau \left( \mu^{m+1}, \mu^{m+1} \right)_{\Gamma^m}^h \leq 0. \end{aligned} \quad (4.12)$$

This implies the energy dissipation property of the SP-PFEM (3.7) as claimed.  $\square$

#### 4.2. Existence of the minimal stabilizing function

In this section, we analyze the existence of the minimal stabilizing function  $k_{\min}^\alpha(\theta)$ .

Assume that  $\hat{\gamma}(\theta) \in C^2(2\pi\mathbb{T})$  satisfies

$$3\hat{\gamma}(\theta) - \hat{\gamma}(\theta - \pi) \geq 0, \quad \forall \theta \in 2\pi\mathbb{T}, \quad (4.13)$$

and let  $c := \inf_{\theta \in 2\pi\mathbb{T}} [3\hat{\gamma}(\theta) - \hat{\gamma}(\theta - \pi)]$ . Since  $k_{\min}^\alpha(\theta) = k_0^\alpha(\theta) - (\alpha-1)\hat{\gamma}(\theta)$ , the existence of  $k_{\min}^\alpha(\theta)$  is equivalent to the boundedness of  $k_0^\alpha(\theta)$ . We therefore focus on the latter. Specifically, we establish a necessary and sufficient condition for the boundedness of  $k_0^\alpha(\theta)$  in the critical case where  $c = 0$ , and derive an upper bound estimate for  $k_0^\alpha(\theta)$  when  $c > 0$ .

##### 4.2.1. Boundedness of $k_0^\alpha(\theta)$

**Theorem 4.1.** *If  $c = 0$ , then  $k_0^\alpha(\theta)$  exists if and only if one of the following conditions holds:*

1.  $\alpha = -1$ ;
2.  $\hat{\gamma}'(\theta^*) = 0$  whenever  $3\hat{\gamma}(\theta^*) = \hat{\gamma}(\theta^* - \pi)$ .

*Proof. Sufficiency.* The proofs for conditions (1) and (2) follow arguments similar to those in [47] and [62], respectively, and are omitted for brevity.

*Necessity.* Suppose  $3\hat{\gamma}(\theta^*) = \hat{\gamma}(\theta^* - \pi)$  for some  $\theta^* \in 2\pi\mathbb{T}$ . Then  $\hat{\gamma}(\theta - \pi)/\hat{\gamma}(\theta)$  attains its maximum at  $\theta = \theta^*$ , which implies

$$\left. \frac{d}{d\theta} \left( \frac{\hat{\gamma}(\theta - \pi)}{\hat{\gamma}(\theta)} \right) \right|_{\theta=\theta^*} = \frac{\hat{\gamma}'(\theta^* - \pi)\hat{\gamma}(\theta^*) - \hat{\gamma}(\theta^* - \pi)\hat{\gamma}'(\theta^*)}{\hat{\gamma}^2(\theta^*)} = \frac{\hat{\gamma}'(\theta^* - \pi) - 3\hat{\gamma}'(\theta^*)}{\hat{\gamma}(\theta^*)} = 0. \quad (4.14)$$

Thus

$$3\hat{\gamma}'(\theta^*) = \hat{\gamma}'(\theta^* - \pi) \quad \text{whenever} \quad 3\hat{\gamma}(\theta^*) = \hat{\gamma}(\theta^* - \pi). \quad (4.15)$$

Define  $F_\alpha(\phi, \theta) := 4\hat{\gamma}(\theta)P_{\alpha, k_{\min}^\alpha}(\phi, \theta) - Q_\alpha^2(\phi, \theta)$ , we have

$$F_\alpha(\phi, \theta) \geq 0, \quad \forall \phi, \theta \in 2\pi\mathbb{T}. \quad (4.16)$$

Applying the mean value theorem to  $F_\alpha(\phi, \theta^*)$  at  $\phi = \pi$ , we have

$$\begin{aligned} F_\alpha(\phi, \theta^*) &= (3\hat{\gamma}(\theta^*) - \hat{\gamma}(\theta^* - \pi))(\hat{\gamma}(\theta^*) + \hat{\gamma}(\theta^* - \pi)) \\ &\quad + [4(\alpha - 1)\hat{\gamma}(\theta^*)\hat{\gamma}'(\theta^*) + 2(\hat{\gamma}(\theta^* - \pi) - \hat{\gamma}(\theta^*))(\hat{\gamma}'(\theta^* - \pi) + \alpha\hat{\gamma}'(\theta^*))](\phi - \pi) \\ &\quad + O((\phi - \pi)^2). \end{aligned} \quad (4.17)$$

Substituting  $3\hat{\gamma}(\theta^*) = \hat{\gamma}(\theta^* - \pi)$  and (4.15) into (4.17), we obtain

$$\begin{aligned} F_\alpha(\phi, \theta^*) &= [4(\alpha - 1)\hat{\gamma}(\theta^*)\hat{\gamma}'(\theta^*) + 2(3\hat{\gamma}(\theta^*) - \hat{\gamma}(\theta^*))(\hat{\gamma}'(\theta^*) + \alpha\hat{\gamma}'(\theta^*))](\phi - \pi) + O((\phi - \pi)^2) \\ &= 8(\alpha + 1)\hat{\gamma}(\theta^*)\hat{\gamma}'(\theta^*)(\phi - \pi) + O((\phi - \pi)^2). \end{aligned} \quad (4.18)$$

Therefore,  $(\alpha + 1)\hat{\gamma}'(\theta^*) = 0$ , yielding either  $\alpha = -1$  or  $\hat{\gamma}'(\theta^*) = 0$ .  $\square$

Theorem 4.1 unifies the main results from [62] and [47], and reveals that  $\alpha = -1$  is the optimal choice among all surface energy matrices. Indeed, as noted in Remark 4.1, condition (3.11)  $3\hat{\gamma}(\theta) - \hat{\gamma}(\theta - \pi) \geq 0$  is both necessary and sufficient for the local energy estimate when  $\alpha = -1$ . In contrast, for  $\alpha \neq -1$ , ensuring energy stability of SP-PFEM under condition (3.11) requires either additional assumptions such as  $\hat{\gamma}'(\theta^*) = 0$ , or strengthening the condition to (3.13)  $3\hat{\gamma}(\theta) - \hat{\gamma}(\theta - \pi) > 0$ .

#### 4.2.2. A global upper bound of $k_0^\alpha(\theta)$

To establish a global upper bound of  $k_0^\alpha(\theta)$ , we introduce the following lemmas:

**Lemma 4.2** ([47]). *Let  $f$  be a non-negative  $C^2$  function on  $2\pi\mathbb{T}$ . Then for any positive constant  $C \geq \sup_{2\pi\mathbb{T}} |f''|$ , we have*

$$-f(x) \leq f'(x)y + \frac{C}{2}y^2, \quad \forall x, y \in 2\pi\mathbb{T}. \quad (4.19)$$

**Lemma 4.3** (Estimation of  $Q_\alpha(\phi, \theta)$ ). *Suppose  $c > 0$ . Then for  $Q_\alpha(\phi, \theta)$  defined in (4.3b), we have*

$$|Q_\alpha(\phi, \theta)| \leq |P_{\alpha, A}(\phi, \theta) + \hat{\gamma}(\theta)|, \quad \forall \phi \in 2\pi\mathbb{T}, \quad (4.20)$$

where  $A(\theta)$  is defined as

$$A(\theta) := \frac{\pi^2}{8} \left( C_\alpha \sup_{2\pi\mathbb{T}} |\hat{\gamma}''| + (3|\alpha| + 2)|\hat{\gamma}'(\theta)| + \hat{\gamma}(\theta) + B(\theta) \right), \quad (4.21a)$$

$$B(\theta) := \frac{2}{c}(\alpha + 1)^2 |\hat{\gamma}'(\theta)|^2, \quad C_\alpha = \max\left\{5, \frac{4}{\pi^2}(2|\alpha| + 1)^2\right\}. \quad (4.21b)$$

*Proof.* We begin by proving the lower bound of  $Q_\alpha(\phi, \theta)$ . Applying Lemma 4.2, we obtain

$$\begin{aligned}
Q_\alpha(\phi, \theta) + P_{\alpha,0}(\phi, \theta) + \hat{\gamma}(\theta) &= \hat{\gamma}(\theta - \phi) + \hat{\gamma}(\theta)(2 + \cos \phi) + \hat{\gamma}'(\theta)\left(\alpha \sin \phi + \frac{\alpha - 1}{2} \sin 2\phi\right) \\
&\geq \hat{\gamma}(\theta) + \hat{\gamma}'(\theta)(\alpha + (\alpha - 1) \cos \phi) \sin \phi \\
&\geq \hat{\gamma}(\theta) - (2|\alpha| + 1)|\hat{\gamma}'(\theta)| \sin \phi \\
&\geq -\frac{(2|\alpha| + 1)^2}{2} \sup_{2\pi\mathbb{T}} |\hat{\gamma}''| \sin^2 \phi.
\end{aligned} \tag{4.22}$$

Combining with the facts  $A(\theta) \geq \frac{(2|\alpha|+1)^2}{2} \sup_{2\pi\mathbb{T}} |\hat{\gamma}''|$  and noting  $P_{\alpha,A}(\phi, \theta) = P_{\alpha,0}(\phi, \theta) + A(\theta) \sin^2 \phi$ , we deduce

$$Q_\alpha(\phi, \theta) \geq -P_{\alpha,0}(\phi, \theta) - \hat{\gamma}(\theta) - A(\theta) \sin^2 \phi = -P_{\alpha,A}(\phi, \theta) - \hat{\gamma}(\theta), \quad \forall \phi \in 2\pi\mathbb{T}. \tag{4.23}$$

The remaining task is to determine the upper bound of  $Q_\alpha(\phi, \theta)$ . We divide the proof into two cases:

Case 1: For  $|\phi| \leq \frac{\pi}{2}$ . By adopting the mean value theorem to  $Q_\alpha(\cdot, \theta) - P_{\alpha,0}(\cdot, \theta) - \hat{\gamma}(\theta)$  on  $[0, \phi]$ , then there exists a  $\xi \in [0, \phi]$  such that

$$\begin{aligned}
Q_\alpha(\phi, \theta) - P_{\alpha,0}(\phi, \theta) - \hat{\gamma}(\theta) &= \frac{1}{2} (\hat{\gamma}''(\theta - \xi) - \hat{\gamma}(\theta) \cos \xi - \alpha \hat{\gamma}'(\theta) \sin \xi + 2(\alpha - 1) \hat{\gamma}'(\theta) \sin 2\xi) \phi^2 \\
&\leq \frac{1}{2} \left( \sup_{2\pi\mathbb{T}} |\hat{\gamma}''| + (3|\alpha| + 2)|\hat{\gamma}'(\theta)| + \hat{\gamma}(\theta) \right) \left( \frac{\pi^2}{4} \sin^2 \phi \right) \\
&\leq A(\theta) \sin^2 \phi.
\end{aligned} \tag{4.24}$$

The penultimate inequality comes from the fact that  $|\phi| \leq \frac{\pi}{2} |\sin \phi|$ ,  $\forall |\phi| \leq \frac{\pi}{2}$ .

Case 2: For  $|\phi - \pi| < \frac{\pi}{2}$ . Again, we apply the mean value theorem to  $Q_\alpha(\cdot, \theta) - P_{\alpha,0}(\cdot, \theta) - \hat{\gamma}(\theta)$  on  $[\phi, \pi]$ . Then there exists a  $\xi \in [\phi, \pi]$  such that

$$\begin{aligned}
Q_\alpha(\phi, \theta) - P_{\alpha,0}(\phi, \theta) - \hat{\gamma}(\theta) &= (\hat{\gamma}(\theta - \pi) - 3\hat{\gamma}(\theta)) - (\hat{\gamma}'(\theta - \pi) + (2\alpha - 1)\hat{\gamma}'(\theta)) (\phi - \pi) \\
&\quad + \frac{1}{2} (\hat{\gamma}''(\theta - \xi) - \hat{\gamma}(\theta) \cos \xi - \alpha \hat{\gamma}'(\theta) \sin \xi + 2(\alpha - 1) \hat{\gamma}'(\theta) \sin 2\xi) (\phi - \pi)^2.
\end{aligned}$$

By the definition of  $c$ , we have  $3\hat{\gamma}(\theta) - \hat{\gamma}(\theta - \pi) \geq c$ . Applying Lemma 4.2 to  $3\hat{\gamma}(\theta) - \hat{\gamma}(\theta - \pi) - c$ , we obtain

$$\begin{aligned}
\hat{\gamma}(\theta - \pi) - 3\hat{\gamma}(\theta) &= -c - (3\hat{\gamma}(\theta) - \hat{\gamma}(\theta - \pi) - c) - c \\
&\leq -c + (\hat{\gamma}'(\theta - \pi) - 3\hat{\gamma}(\theta)) (\phi - \pi) + \frac{1}{2} \sup_{2\pi\mathbb{T}} |3\hat{\gamma}''(\theta) - \hat{\gamma}''(\theta - \pi)| (\phi - \pi)^2 \\
&\leq -c + (\hat{\gamma}'(\theta - \pi) - 3\hat{\gamma}(\theta)) (\phi - \pi) + 2 \sup_{2\pi\mathbb{T}} |\hat{\gamma}''| (\phi - \pi)^2.
\end{aligned} \tag{4.25}$$

Therefore,

$$\begin{aligned}
Q_\alpha(\phi, \theta) - P_{\alpha,0}(\phi, \theta) - \hat{\gamma}(\theta) &\leq -c + (\hat{\gamma}'(\theta - \pi) - 3\hat{\gamma}(\theta)) (\phi - \pi) + 2 \sup_{2\pi\mathbb{T}} |\hat{\gamma}''| (\phi - \pi)^2 - (\hat{\gamma}'(\theta - \pi) + (2\alpha - 1)\hat{\gamma}'(\theta)) (\phi - \pi) \\
&\quad + \frac{1}{2} (\hat{\gamma}''(\theta - \xi) - \hat{\gamma}(\theta) \cos \xi - \alpha \hat{\gamma}'(\theta) \sin \xi + 2(\alpha - 1) \hat{\gamma}'(\theta) \sin 2\xi) (\phi - \pi)^2 \\
&\leq -c - 2(\alpha + 1)\hat{\gamma}'(\theta)(\phi - \pi) + \frac{1}{2} \left( 5 \sup_{2\pi\mathbb{T}} |\hat{\gamma}''| + (3|\alpha| + 2)|\hat{\gamma}'(\theta)| + \hat{\gamma}(\theta) \right) (\phi - \pi)^2.
\end{aligned} \tag{4.26}$$

Since  $c > 0$ , the lower order term in the right-hand side of (4.26) can be controlled by a quadratic term, i.e.

$$-c - 2(\alpha + 1)\hat{\gamma}'(\theta)(\phi - \pi) \leq \frac{1}{c}(\alpha + 1)^2 |\hat{\gamma}'(\theta)|^2 (\phi - \pi)^2. \tag{4.27}$$

Combining with the fact that  $|\phi - \pi| \leq \frac{\pi}{2} |\sin \phi|$ ,  $\forall |\phi - \pi| \leq \frac{\pi}{2}$ , we obtain the desired inequality

$$Q_\alpha(\phi, \theta) \leq P_{\alpha,A}(\phi, \theta) + \hat{\gamma}(\theta), \quad \forall \phi \in 2\pi\mathbb{T}. \quad (4.28)$$

□

**Theorem 4.2.** *If  $c > 0$ . For any  $\alpha \in \mathbb{R}$ ,  $k_0^\alpha(\theta)$  given in (4.1) admits the following upper bound:*

$$k_0^\alpha(\theta) \leq \frac{1}{4\hat{\gamma}(\theta)} [A^2(\theta) + 4\hat{\gamma}(\theta)A(\theta) + (\alpha - 1)^2|\hat{\gamma}'(\theta)|^2] < +\infty, \quad \forall \theta \in 2\pi\mathbb{T}. \quad (4.29)$$

*Proof.* By Lemma 4.3, we have

$$Q_\alpha^2(\phi, \theta) \leq (P_{\alpha,A}(\phi, \theta) + \hat{\gamma}(\theta))^2, \quad \forall \phi \in 2\pi\mathbb{T}. \quad (4.30)$$

Recall the definition of  $P_{\alpha,a}(\phi, \theta)$  in (4.3a), we know that  $P_{\alpha,a}(\phi, \theta) = P_{\alpha,0}(\phi, \theta) + a(\theta) \sin^2 \phi$ . Thus,

$$\begin{aligned} 4\hat{\gamma}(\theta)P_{\alpha,a}(\phi, \theta) - Q_\alpha^2(\phi, \theta) &\geq 4\hat{\gamma}(\theta)(a(\theta) - A(\theta)) \sin^2 \phi + 4\hat{\gamma}(\theta)P_{\alpha,A}(\phi, \theta) - (P_{\alpha,A}(\phi, \theta) + \hat{\gamma}(\theta))^2 \\ &= 4\hat{\gamma}(\theta)(a(\theta) - A(\theta)) \sin^2 \phi - (P_{\alpha,A}(\phi, \theta) - \hat{\gamma}(\theta))^2 \\ &= (4\hat{\gamma}(\theta)(a(\theta) - A(\theta)) - ((\alpha - 1)\hat{\gamma}'(\theta) \cos \phi + A(\theta) \sin \phi)^2) \sin^2 \phi \\ &\geq (4\hat{\gamma}(\theta)a(\theta) - A^2(\theta) - (\alpha - 1)^2|\hat{\gamma}'(\theta)|^2 - 4\hat{\gamma}(\theta)A(\theta)) \sin^2 \phi. \end{aligned} \quad (4.31)$$

The last inequality is a direct consequence of the bound  $|a \cos \phi + b \sin \phi| \leq \sqrt{a^2 + b^2}$ ,  $\forall \phi \in 2\pi\mathbb{T}$ .

Therefore, for any  $a(\theta) \geq \frac{1}{4\hat{\gamma}(\theta)} [A^2(\theta) + 4\hat{\gamma}(\theta)A(\theta) + (\alpha - 1)^2|\hat{\gamma}'(\theta)|^2]$ , we have

$$4\hat{\gamma}(\theta)P_{\alpha,a}(\phi, \theta) - Q_\alpha^2(\phi, \theta) \geq 0, \quad \forall \phi \in 2\pi\mathbb{T}. \quad (4.32)$$

This gives (4.29) by the definition of  $k_0^\alpha(\theta)$  in (4.2), and the proof is complete. □

## 5. Generalizations to other geometric flows

In this section, we consider two specific geometric flows, namely the area-conserved anisotropic curvature flow and the anisotropic surface diffusion, and present their corresponding SP-PFEMs. At the end of this section, based on the proposed analytical framework, we will discuss how to design structure-preserving algorithms for general normal velocity laws.

### 5.1. Area-conserved anisotropic curvature flow

Similar to (2.9), for the area-conserved anisotropic curvature flow in (1.3), we have the following conservative strong formulation:

$$\mathbf{n} \cdot \partial_t \mathbf{X} + \mu - \lambda(t) = 0, \quad (5.1a)$$

$$\mu \mathbf{n} + \partial_s \left( \hat{\mathbf{G}}_k^\alpha(\theta) \partial_s \mathbf{X} \right) = \mathbf{0}, \quad (5.1b)$$

where  $\lambda(t) := \int_{\Gamma(t)} \mu \, ds / |\Gamma(t)|$  is the Lagrange multiplier that ensures the enclosed area remains constant over time.

Suppose the initial closed curve  $\Gamma(0) = \mathbf{X}(\cdot, 0) \in [H_p^1(\mathbb{I})]^2$  and the initial weighted curvature  $\mu(\cdot, 0) = \mu_0(\cdot) \in H_p^1(\mathbb{I})$  is given. Then a variational formulation based on (5.1) is stated as follows: For any  $t > 0$ , find the solution  $(\mathbf{X}(\cdot, t), \mu(\cdot, t)) \in [H_p^1(\mathbb{I})]^2 \times H_p^1(\mathbb{I})$  such that

$$\left( \mathbf{n} \cdot \partial_t \mathbf{X}, \varphi \right)_{\Gamma(t)} + \left( \mu - \lambda(t), \varphi \right)_{\Gamma(t)} = 0, \quad \forall \varphi \in [H_p^1(\mathbb{I})]^2, \quad (5.2a)$$

$$\left( \mu \mathbf{n}, \boldsymbol{\omega} \right)_{\Gamma(t)} - \left( \hat{\mathbf{G}}_k^\alpha(\theta) \partial_s \mathbf{X}, \partial_s \boldsymbol{\omega} \right)_{\Gamma(t)} = 0, \quad \forall \boldsymbol{\omega} \in [H_p^1(\mathbb{I})]^2. \quad (5.2b)$$

Then the SP-PFEM for area-conserved anisotropic curvature flow in (1.3) is as follows: Suppose the initial curve  $\Gamma^0$  is given by  $\mathbf{X}^0(\rho_j) = \mathbf{X}(\rho_j, 0)$ ,  $j = 1, 2, \dots, N$ . For any  $m \geq 0$ , find the solution  $(\mathbf{X}^{m+1}(\cdot), \mu^{m+1}(\cdot)) \in [\mathbb{K}_p^h]^2 \times \mathbb{K}_p^h$  such that

$$\left( \mathbf{n}^{m+\frac{1}{2}} \cdot \frac{\mathbf{X}^{m+1} - \mathbf{X}^m}{\tau}, \varphi^h \right)_{\Gamma^m}^h + \left( \mu^{m+1} - \lambda^{m,*}, \varphi^h \right)_{\Gamma^m}^h = 0, \quad \forall \varphi^h \in \mathbb{K}_p^h, \quad (5.3a)$$

$$\left( \mu^{m+1} \mathbf{n}^{m+\frac{1}{2}}, \boldsymbol{\omega}^h \right)_{\Gamma^m}^h - \left( \hat{\mathbf{G}}_k^\alpha(\theta^m) \partial_s \mathbf{X}^{m+1}, \partial_s \boldsymbol{\omega}^h \right)_{\Gamma^m}^h = 0, \quad \forall \boldsymbol{\omega}^h \in [\mathbb{K}_p^h]^2, \quad (5.3b)$$

where  $\lambda^{m,*} := (\mu^{m+1}, 1)_{\Gamma^m}^h / |\Gamma^m|$ .

For the SP-PFEM (5.3), we have the following structure-preserving property:

**Theorem 5.1.** *Suppose  $\hat{\gamma}(\theta)$  satisfies (3.13) or (3.11) when  $a = -1$ . Then the SP-PFEM (5.3) is structure-preserving with sufficiently large  $k(\theta)$ , i.e.*

$$A^{m+1} = A^m = \dots = A^0, \quad W^{m+1} \leq W^m \leq \dots \leq W^0, \quad \forall m \geq 0. \quad (5.4)$$

The proof is similar to that in [4, Theorem 4.2] and is therefore omitted.

### 5.2. Anisotropic surface diffusion

Similarly, for anisotropic surface diffusion in (1.3), the conservative strong form is given as

$$\mathbf{n} \cdot \partial_t \mathbf{X} - \partial_{ss} \mu = 0, \quad (5.5a)$$

$$\mu \mathbf{n} + \partial_s \left( \hat{\mathbf{G}}_k^\alpha(\theta) \partial_s \mathbf{X} \right) = \mathbf{0}. \quad (5.5b)$$

And the corresponding variational formulation follows by a similar derivation.

Suppose the initial closed curve  $\Gamma^0$  is given by  $\mathbf{X}^0(\rho_j) = \mathbf{X}(\rho_j, 0)$ ,  $j = 1, 2, \dots, N$ . Then the SP-PFEM for anisotropic surface diffusion in (1.3) can be stated as follows: For  $m \geq 0$ , find the solution  $(\mathbf{X}^{m+1}(\cdot), \mu^{m+1}(\cdot)) \in [\mathbb{K}_p^h]^2 \times \mathbb{K}_p^h$  satisfying

$$\left( \mathbf{n}^{m+\frac{1}{2}} \cdot \frac{\mathbf{X}^{m+1} - \mathbf{X}^m}{\tau}, \varphi^h \right)_{\Gamma^m}^h + \left( \partial_s \mu^{m+1}, \partial_s \varphi^h \right)_{\Gamma^m}^h = 0, \quad \forall \varphi^h \in \mathbb{K}_p^h, \quad (5.6a)$$

$$\left( \mu^{m+1} \mathbf{n}^{m+\frac{1}{2}}, \boldsymbol{\omega}^h \right)_{\Gamma^m}^h - \left( \hat{\mathbf{G}}_k^\alpha(\theta^m) \partial_s \mathbf{X}^{m+1}, \partial_s \boldsymbol{\omega}^h \right)_{\Gamma^m}^h = 0, \quad \forall \boldsymbol{\omega}^h \in [\mathbb{K}_p^h]^2. \quad (5.6b)$$

For the SP-PFEM (5.6), the following structure-preserving property holds:

**Theorem 5.2.** *Suppose  $\hat{\gamma}(\theta)$  satisfies (3.13) or (3.11) when  $a = -1$ . Then the SP-PFEM (5.6) is structure-preserving with sufficiently large  $k(\theta)$ , i.e.*

$$A^{m+1} = A^m = \dots = A^0, \quad W^{m+1} \leq W^m \leq \dots \leq W^0, \quad \forall m \geq 0. \quad (5.7)$$

For the proof we refer the reader to [47]. Details are omitted here for brevity.

### 5.3. General normal velocity laws

The introduction of surface energy matrices enables us to address anisotropic problems analogously to the way isotropic cases are treated in the BGN-type method.

Here we consider flows of the form

$$V_n = \mathfrak{F}(\mu), \quad \text{on } \Gamma(t), \quad (5.8)$$

where  $\mathfrak{F}(\cdot)$  is a mapping that maps functions on closed evolving curve  $\Gamma(t)$  to functions on  $\Gamma(t)$ .

If  $\mathfrak{F}$  satisfies

$$\left( \mathfrak{F}(\mu), \mu \right)_{\Gamma(t)} \leq 0, \quad (5.9)$$

then the evolution equation (5.8) exhibits the property of area decay rate and energy dissipation as

$$\frac{d}{dt}A(t) = \left( \mathfrak{F}(\mu), 1 \right)_{\Gamma(t)}, \quad \frac{d}{dt}W(t) = \left( V_n, \mu \right)_{\Gamma(t)} = \left( \mathfrak{F}(\mu), \mu \right)_{\Gamma(t)} \leq 0. \quad (5.10)$$

All the evolution laws discussed above can be incorporated into this equation. For instance, for the anisotropic surface diffusion  $V_n = \partial_{ss}\mu$ , by taking integration by parts, we have

$$\left( \mathfrak{F}(\mu), \mu \right)_{\Gamma(t)} = \left( \partial_{ss}\mu, \mu \right)_{\Gamma(t)} = - \left( \partial_s\mu, \partial_s\mu \right)_{\Gamma(t)} \leq 0. \quad (5.11)$$

As we have seen earlier, to obtain a structure-preserving numerical scheme for the evolution equation (5.8), we should formally consider the following strong form:

$$\mathbf{n} \cdot \partial_t \mathbf{X} - \mathfrak{F}(\mu) = 0, \quad (5.12a)$$

$$\mu \mathbf{n} + \partial_s \left( \hat{\mathbf{G}}_k^\alpha(\theta) \partial_s \mathbf{X} \right) = \mathbf{0}. \quad (5.12b)$$

While the notation  $\mathfrak{F}(\mu)$  is conventional, constructing structure-preserving fully discrete schemes requires careful treatment of the underlying curve  $\Gamma(t)$ . To make this dependence explicit, we adopt the notation  $\mathfrak{F}(\mu, \Gamma) = \mathfrak{F}(\mu)$ . This perspective naturally suggests a semi-implicit discretization: treating  $\mu$  implicitly at time level  $m+1$  while treating  $\Gamma$  explicitly at level  $m$ . As shown below, this strategy yields structure-preserving fully discrete schemes in a unified manner:

Suppose the initial data  $\Gamma^0$  is given. For  $m \geq 0$ , find the solution  $(\mathbf{X}^{m+1}(\cdot), \mu^{m+1}(\cdot)) \in [\mathbb{K}_p^h]^2 \times \mathbb{K}_p^h$  such that

$$\left( \mathbf{n}^{m+\frac{1}{2}} \cdot \frac{\mathbf{X}^{m+1} - \mathbf{X}^m}{\tau}, \varphi^h \right)_{\Gamma^m} - \left( \mathfrak{F}(\mu^{m+1}, \Gamma^m), \varphi^h \right)_{\Gamma^m} = 0, \quad \forall \varphi^h \in \mathbb{K}_p^h, \quad (5.13a)$$

$$\left( \mu^{m+1} \mathbf{n}^{m+\frac{1}{2}}, \boldsymbol{\omega}^h \right)_{\Gamma^m} - \left( \hat{\mathbf{G}}_k^\alpha(\theta^m) \partial_s \mathbf{X}^{m+1}, \partial_s \boldsymbol{\omega}^h \right)_{\Gamma^m} = 0, \quad \forall \boldsymbol{\omega}^h \in [\mathbb{K}_p^h]^2. \quad (5.13b)$$

For (5.13), the following structure-preserving property holds:

**Theorem 5.3.** *Suppose  $\hat{\gamma}(\theta)$  satisfies (3.13) or (3.11) when  $a = -1$ . Then the SP-PFEM (5.13) is structure-preserving with sufficiently large  $k(\theta)$ , i.e.*

$$\frac{A^{m+1} - A^m}{\tau} = - \left( \mathfrak{F}(\mu^{m+1}, \Gamma^m), 1 \right)_{\Gamma^m}^h, \quad W^{m+1} \leq W^m \leq \dots \leq W^0, \quad \forall m \geq 0. \quad (5.14)$$

*Proof.* For the area decay rate. Similar to (3.14), we have

$$A^{m+1} - A^m = \left( \mathbf{n}^{m+\frac{1}{2}} \cdot (\mathbf{X}^{m+1} - \mathbf{X}^m), 1 \right)_{\Gamma^m}^h = -\tau \left( \mathfrak{F}(\mu^{m+1}, \Gamma^m), 1 \right)_{\Gamma^m}^h. \quad (5.15)$$

For the energy dissipation, (4.11) still holds. Thus, we have

$$\begin{aligned} W^{m+1} - W^m &\leq \left( \hat{\mathbf{G}}_k^\alpha(\theta^m) \partial_s \mathbf{X}^{m+1}, \partial_s (\mathbf{X}^{m+1} - \mathbf{X}^m) \right)_{\Gamma^m}^h \\ &= \left( \mu^{m+1} \mathbf{n}^{m+\frac{1}{2}}, \mathbf{X}^{m+1} - \mathbf{X}^m \right)_{\Gamma^m}^h = -\tau \left( \mathfrak{F}(\mu^{m+1}, \Gamma^m), \mu^{m+1} \right)_{\Gamma^m}^h \leq 0. \end{aligned} \quad (5.16)$$

The last inequality follows from the assumption (5.9).  $\square$

Here, we present three examples to illustrate our ideas. For additional examples and numerical discussions, we refer the reader to [18, section 5] by Barrett et al. as well as the references therein.

**Example 5.1.** *By choosing  $\mathfrak{F}(f, \Gamma) = -f + \int_\Gamma f \, ds / |\Gamma|$ , where  $f$  is a function on  $\Gamma$ , we obtain  $\mathfrak{F}(\mu^{m+1}, \Gamma^m) = -\mu^{m+1} + \int_{\Gamma^m} \mu^{m+1} \, ds / |\Gamma^m|$ . This leads to the SP-PFEM for the area-conserved anisotropic curvature flow, as shown in (5.3).*

**Example 5.2.** For the surface diffusion, we take  $\mathfrak{F}(f, \Gamma) = -\partial_{ss}f$ , where  $\partial_s$  denotes differentiation with respect to arc-length along  $\Gamma$ . Applying integration by parts yields  $(\mathfrak{F}(\mu, \Gamma), \mu)_\Gamma = -(\partial_s\mu, \partial_s\mu)_\Gamma \leq 0$ , which leads to recovery of the SP-PFEM (5.6) and Theorem 5.2 for anisotropic surface diffusion.

**Example 5.3.** An intermediate flow between the area-conserved anisotropic curvature flow and surface diffusion is

$$V_n = \partial_{ss}\eta, \quad \text{where} \quad \left(-\frac{1}{\xi}\partial_{ss} + \frac{1}{\nu}\right)\eta = \mu, \quad (5.17)$$

and  $\xi, \nu \in \mathbb{R}^+$ . We define the mapping  $\mathfrak{F}(\cdot, \Gamma^m)$  via

$$\left(\mathfrak{F}(f, \Gamma^m), \varphi^h\right)_{\Gamma^m}^h = \left(\partial_s\eta(f), \partial_s\varphi^h\right)_{\Gamma^m}^h, \quad \forall \varphi^h \in \mathbb{K}_p^h, \quad (5.18)$$

where  $\eta(f)$  represents the solution of

$$\frac{1}{\xi}\left(\partial_s\eta(f), \partial_s\psi^h\right)_{\Gamma^m}^h + \frac{1}{\nu}\left(\eta(f), \psi^h\right)_{\Gamma^m}^h = \left(f, \psi^h\right)_{\Gamma^m}^h, \quad \forall \psi^h \in \mathbb{K}_p^h. \quad (5.19)$$

Taking  $f = \varphi^h = \mu^{m+1}$ ,  $\psi^h = \mu^{m+1} - \frac{1}{\nu}\eta(\mu^{m+1})$ , we obtain

$$\left(\mathfrak{F}(\mu^{m+1}, \Gamma^m), \mu^{m+1}\right)_{\Gamma^m}^h = -\frac{1}{\nu}\left(\eta, \eta\right)_{\Gamma^m}^h - \xi\left(\mu^{m+1} - \frac{1}{\nu}\eta, \mu^{m+1} - \frac{1}{\nu}\eta\right)_{\Gamma^m}^h \leq 0. \quad (5.20)$$

As a result, we will derive a structure-preserving discretization of the intermediate flow (5.17) under the condition (3.13) or (3.11). For further discussion of the intermediate flow, we refer the reader to [31, 32, 56] for theoretical aspects and to [10, 12] for numerical methods.

## 6. Numerical results

In this section, we will report extensive numerical experiments to demonstrate the high performance of the proposed SP-PFEMs.

### 6.1. Error and convergence rate

To measure the distance between two closed curves  $\Gamma_1$  and  $\Gamma_2$ , we introduce the manifold distance  $M(\Gamma_1, \Gamma_2)$  as follows [46, 63]:

$$M(\Gamma_1, \Gamma_2) := |(\Omega_1 \setminus \Omega_2) \cup (\Omega_2 \setminus \Omega_1)| = 2|\Omega_1 \cup \Omega_2| - |\Omega_1| - |\Omega_2|, \quad (6.1)$$

where  $\Omega_i$  ( $i = 1, 2$ ) is the interior region enclosed by  $\Gamma_i$  and  $|\Omega|$  denotes the area of  $\Omega$ .

We define the intermediate curve  $\Gamma_{h,\tau}(t)$  between  $\Gamma^m, \Gamma^{m+1}$  as

$$\Gamma_{h,\tau}(t) := \frac{t_{m+1} - t}{\tau} \Gamma^m + \frac{t - t_m}{\tau} \Gamma^{m+1}, \quad t \in [t_m, t_{m+1}], \quad m \geq 0. \quad (6.2)$$

The numerical error  $e^h(t)$  is formally given as

$$e^h(t) := M(\Gamma_{h,\tau}(t), \Gamma(t)). \quad (6.3)$$

We approximate the exact solution  $\Gamma(t)$  by  $\Gamma_{h_e, \tau_e}(t)$  with fine meshes  $h_e = 2^{-8}$ ,  $\tau_e = h_e^2$ .

In the convergence tests, we mainly consider the following two types of surface energies:

- Case I:  $\hat{\gamma}(\theta) = 1 + \beta \cos 3\theta$  with  $|\beta| < 1$ .
- Case II:  $\hat{\gamma}(\theta) = \sqrt{\left(\frac{5}{2} + \frac{3}{2}\text{sgn}(n_1)\right)n_1^2 + n_2^2}$ , where  $\mathbf{n} = (n_1, n_2)^T = (-\sin \theta, \cos \theta)^T$ .

$\alpha$	$(h, \tau)$	$e^h(t = 0.1)$	order	$e^h(t = 0.2)$	order	$e^h(t = 0.3)$	order
-1	$(h_0, \tau_0)$	1.30e-1	-	1.63e-1	-	1.84e-1	-
	$(\frac{h_0}{2}, \frac{\tau_0}{4})$	3.12e-2	2.06	4.03e-2	2.01	4.64e-2	1.98
	$(\frac{h_0}{2^2}, \frac{\tau_0}{4^2})$	8.02e-3	1.96	1.05e-2	1.94	1.21e-2	1.94
0	$(h_0, \tau_0)$	1.30e-1	-	1.56e-2	-	1.73e-1	-
	$(\frac{h_0}{2}, \frac{\tau_0}{4})$	3.14e-2	2.05	4.04e-2	1.95	4.65e-2	1.90
	$(\frac{h_0}{2^2}, \frac{\tau_0}{4^2})$	8.00e-3	1.97	1.04e-2	1.95	1.20e-2	1.94
1	$(h_0, \tau_0)$	1.31e-1	-	1.58e-1	-	1.76e-1	-
	$(\frac{h_0}{2}, \frac{\tau_0}{4})$	3.15e-2	2.05	4.05e-2	1.97	4.66e-2	1.92
	$(\frac{h_0}{2^2}, \frac{\tau_0}{4^2})$	7.98e-3	1.98	1.04e-2	1.97	1.20e-2	1.96

Table 1: Error  $e^h(t)$  and the convergence rates of SP-PFEM (3.7) with  $\alpha = 0, \pm 1$ . The anisotropy is chosen from the energy density in Case I, with  $\beta$  set to  $1/9$ . Other parameters are chosen as  $h_0 = 2^{-4}, \tau_0 = h_0^2$ .

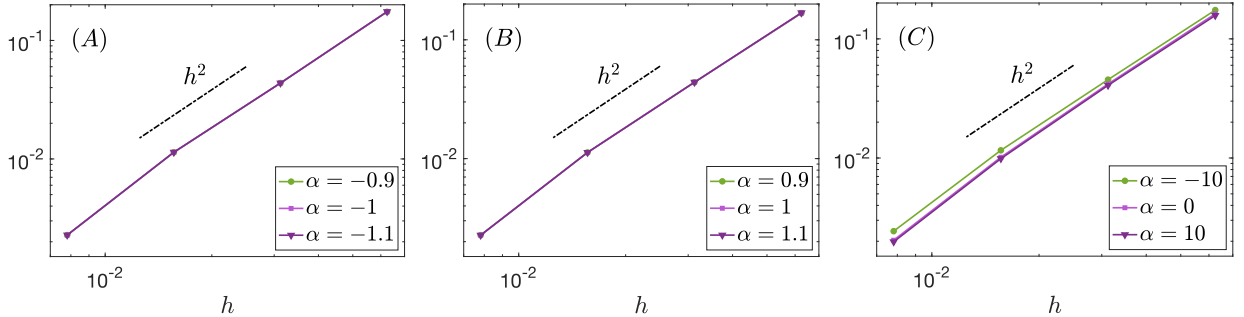


Figure 2: Convergence rates of SP-PFEM (3.7) with different  $\alpha$  at  $t = 0.25$ : (A)–(B) Case I with  $\beta = 1/9$ ; and (C) Case II.

The minimal stabilizing function  $k_{\min}^{\alpha}(\theta)$  is obtained as follows: for a given  $\hat{\gamma}(\theta)$  and  $\alpha \in \mathbb{R}$ , we solve the optimization problem (4.2) at  $\theta_j = -\pi + \frac{j\pi}{10}, \forall 0 \leq j \leq 20$  to compute  $k_0^{\alpha}(\theta_j)$ , then use linear interpolation to approximate  $k_0^{\alpha}(\theta)$  at the intermediate points and obtain  $k_{\min}^{\alpha}(\theta)$  by (4.1). In the following convergence tests, the stabilizing functions are always chosen to be  $k(\theta) = k_{\min}^{\alpha}(\theta)$ , unless otherwise stated.

Given that the numerical scheme formally exhibits second-order spatial accuracy and first-order temporal accuracy, the time step  $\tau$  is consistently chosen as  $\tau = h^2$ , unless otherwise specified. In this subsection, the initial curve is chosen as an ellipse with a major axis of 4 and a minor axis of 1. The tolerance value for the Newton's iteration is set to be  $\text{tol} = 10^{-11}$ .

Numerical errors are reported in Table 1 and Figure 2. It can be observed that the SP-PFEM (3.7) exhibits second-order spatial accuracy and first-order temporal accuracy.

We compared the errors corresponding to multiple different values of  $\alpha$  at the same time  $t = 0.25$  for Case I and Case II, as shown in Figure 3. Specifically, we tested the baseline values  $\alpha = 0, \pm 1$ , values near the baseline  $\alpha = \pm 0.9, \pm 1.1$ , fractional values  $\alpha = \pm 0.5$ , as well as larger values  $\alpha = \pm 3, \pm 6, \pm 10$ . The results indicate that the accuracy of the SP-PFEM (3.7) is robust with respect to the choice of  $\alpha$ . In particular, it was observed that the relative differences among these errors remained below 5% in the majority of cases.

## 6.2. Iteration count and CPU time

Table 2 presents the total number of iterations and the average CPU time for the SP-PFEM (3.7) with different values of  $\alpha$  at the fixed time  $t = 0.1$ . The reported CPU time is computed as the mean over five independent runs. All computations were performed on a personal laptop equipped with an Apple M1 Pro chip and 16GB of RAM, running macOS Sequoia 15.3.2. The data presented in Table 2 show that

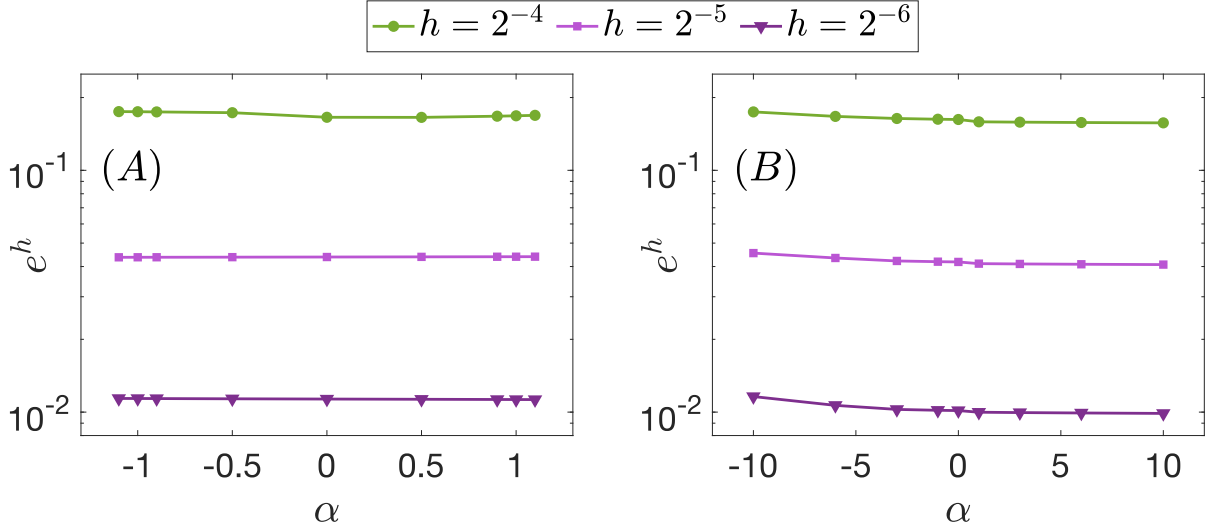


Figure 3: Error comparison of SP-PFEM (3.7) at  $t = 0.25$ : (A) Case I with  $\alpha = 0, \pm 0.5, \pm 0.9, \pm 1, \pm 1.1$ ; and (B) Case II with  $\alpha = 0, \pm 1, \pm 3, \pm 6, \pm 10$ .

$\alpha$	$(h, \tau) = (2^{-7}, 4^{-7})$		$(h, \tau) = (2^{-8}, 4^{-8})$	
	Iteration count	CPU time (s)	Iteration count	CPU time (s)
-10	3278	17.9999	15856	162.2915
-5	3278	18.0083	13265	148.6691
-1	3278	18.5907	13294	151.7395
0	3278	18.6436	13304	152.5232
1	3278	18.3653	13313	151.2127
5	3278	18.6596	13496	151.3283
10	3278	17.1996	18070	166.7016

Table 2: The total number of iterations and average CPU time of SP-PFEM (3.7) for Case I with  $\beta = 1/7$  at  $t = 0.1$ .

the average number of iterations per update step is about 2, indicating that our scheme can be solved by Newton's method with high efficiency. The average CPU time is approximately 18 seconds for mesh  $(h, \tau) = (2^{-7}, 4^{-7})$  and around 150 seconds for the fine mesh  $(h_e, \tau_e) = (2^{-8}, 4^{-8})$ . The results indicate that the SP-PFEM (3.7) exhibits a consistent computational efficiency across different values of  $\alpha$ .

### 6.3. Minimal stabilizing function and mesh quality

#### 6.3.1. Minimal stabilizing function

Figure 4 displays the minimal stabilizing functions for the 3-fold anisotropy  $\hat{\gamma}(\theta) = 1 + \beta \cos 3\theta$  and the variation of the ratios of their  $L^\infty$ -norm to the  $L^\infty$ -norm of  $\hat{\gamma}(\theta)$  with respect to parameter  $\alpha$ . In the right panel, the plot of  $k_0^\alpha$  is provided for  $\alpha = -1$ . It can be observed that the value of  $k_{\min}^\alpha(\theta)$  increases as the anisotropy strength  $\beta$  increases. Moreover, in the critical case  $\beta = \frac{1}{2}$  of condition (3.13) or (3.11),  $k_{\min}^\alpha(\theta)$  remains finite, which is consistent with Theorem 4.1. From the left panel, it can be observed that the supremum of  $k_{\min}^\alpha$  increases rapidly as  $|\alpha|$  becomes larger. When  $-1 \leq \alpha \leq 1$ , the growth is moderate, but once  $|\alpha| > 1$ , the stabilizing term  $k_{\min}^\alpha(\theta)\mathbf{n}(\theta)\mathbf{n}(\theta)^T$  in the surface energy matrix  $\hat{\mathbf{G}}_k^\alpha(\theta)$  becomes significantly larger in magnitude than the other components.

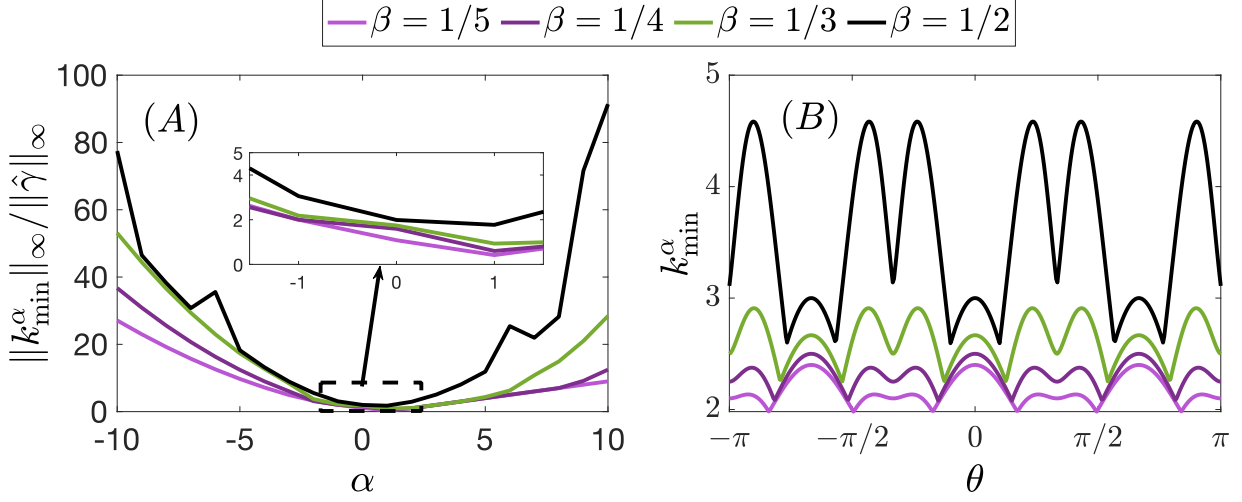


Figure 4: Minimal stabilizing functions and the ratios of their  $L^{\infty}$ -norms to the  $L^{\infty}$ -norm of the anisotropy in Case I.

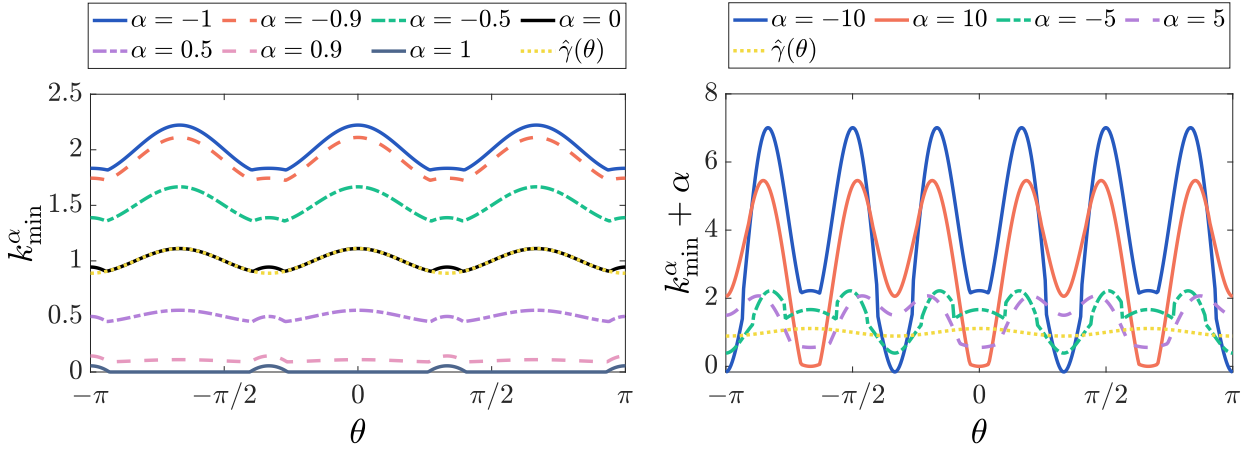


Figure 5: Minimal stabilizing functions for different values of  $\alpha$  in Case I with  $\beta = 1/9$ .

Plots of  $k_{\min}^{\alpha}(\theta)$  and  $k_{\min}^{\alpha}(\theta) + \alpha$  are given in Figure 5 for different values of  $\alpha$ . The left panel shows that, for small  $\alpha$ ,  $k_{\min}^{\alpha}(\theta)$  exhibits an approximately linear dependence on  $\alpha$ . For large values of  $|\alpha|$ , we use  $k_{\min}^{\alpha} + \alpha$  as an indicator of the magnitude of the regularization term in  $\hat{\mathbf{G}}_k^{\alpha}(\theta)$ . As shown in the right panel of Figure 5, the regularization term becomes significantly larger than  $\hat{\gamma}(\theta)$ , which is consistent with the conclusion drawn from Fig. 4.

### 6.3.2. Weighted mesh ratio

To test the mesh quality, we introduce the weighted mesh ratio  $R_{\gamma}^h(t)$  as follows:

$$R_{\gamma}^h(t) \Big|_{t=t_m} := \frac{\max_{1 \leq j \leq N} \hat{\gamma}(\theta_j) |\mathbf{h}_j^m|}{\min_{1 \leq j \leq N} \hat{\gamma}(\theta_j) |\mathbf{h}_j^m|}, \quad m \geq 0. \quad (6.4)$$

As the anisotropic curvature flow causes the curve to collapse into a singularity, we conduct experiments on anisotropic surface diffusion to examine the long-time mesh properties of the proposed method.

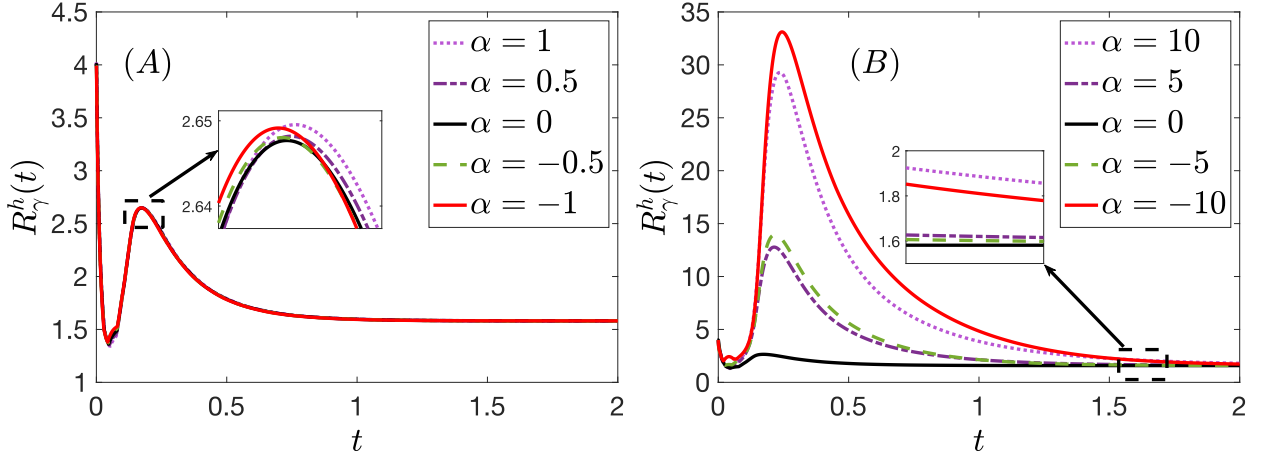


Figure 6: Weighted mesh ratio of the SP-PFEM (5.6) of an ellipse with major axis 4 and minor axis 1 under anisotropic surface diffusion with anisotropy  $\hat{\gamma}(\theta) = 1 + \frac{1}{16} \cos 4\theta$  for different values of  $\alpha$ . The mesh sizes are chosen as  $(h, \tau) = (2^{-6}, 4^{-6})$ .

Figure 6 shows the weighted mesh ratio  $R_\gamma^h(t)$  of the SP-PFEM (5.6) for an ellipse with major axis 4 and minor axis 1 under anisotropic surface diffusion with anisotropy  $\hat{\gamma}(\theta) = 1 + \frac{1}{16} \cos 4\theta$ . The results indicate that the weighted mesh ratio  $R_\gamma^h$  converges to a constant as  $t \rightarrow \infty$ , indicating that the SP-PFEM (5.6) achieves an asymptotically quasi-uniform mesh distribution. Moreover, it can be observed that for small values of  $|\alpha|$ , the behavior of the weighted mesh ratio  $R_\gamma^h$  remains nearly identical. However, when  $|\alpha|$  is large,  $R_\gamma^h$  can become significantly larger during the early stages of evolution. Therefore, to achieve better mesh quality in practical applications, smaller values of  $|\alpha|$  are recommended.

#### 6.4. Area decay rate and energy dissipation

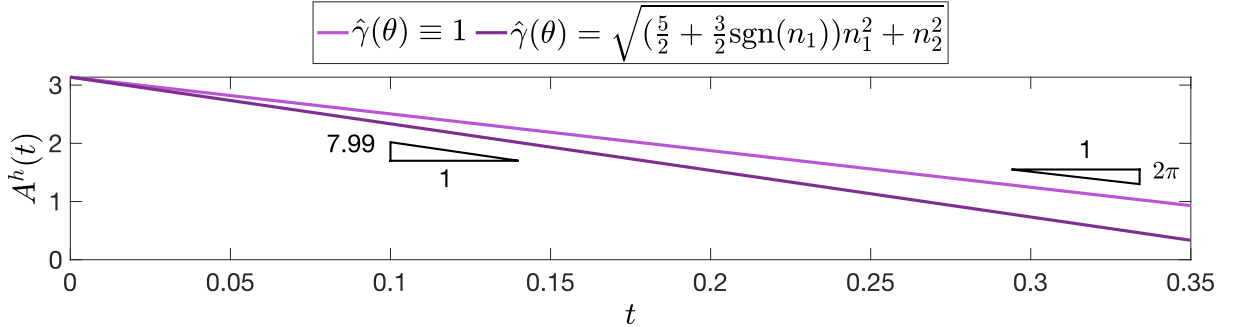


Figure 7: Area and area decay rate of an ellipse with major axis 4 and minor axis 1 under anisotropic curvature flow by SP-PFEM (3.7) with  $\alpha = 0$ .

Figure 7 illustrates the evolution of the area of an ellipse with major axis 4 and minor axis 1 under anisotropic curvature flows by SP-PFEM (3.7) with two surface energy densities: (i) the isotropic surface energy density  $\hat{\gamma}(\theta) \equiv 1$ ; (ii) Case II. It can be observed that the area decreases approximately linearly.

For a simple closed curve evolving under the isotropic curvature flow, the area decay rate  $\frac{dA(t)}{dt} = \int_\Gamma \kappa ds = -2\pi$  remains constant. For anisotropic surface energies, the area decay rate tends to approach a constant value  $-\int_\Gamma \mu ds$ . Here,  $\Gamma$  represents the Wulff shape associated with the anisotropy  $\hat{\gamma}(\theta)$  [50], scaled to have the same enclosed area as the initial curve. In particular, for the surface energy density of Case II, we have  $-\int_\Gamma \mu ds \approx -7.9858$  [4].

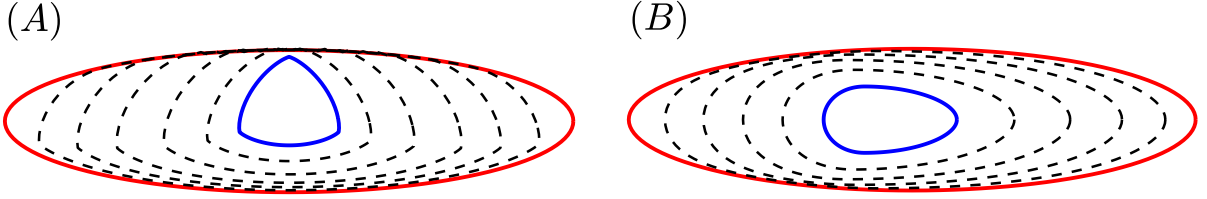


Figure 8: Morphological evolution of an ellipse with major axis 4 and minor axis 1 under anisotropic curvature flow by SP-PFEM (3) for: (A) Case I with  $\beta = 1/7$ ; and (B) Case II. The red lines represent the initial shapes. The blue lines represent the numerical curves at (A)  $t = 0.45$  and (B)  $t = 0.35$ . The black dashed lines represent the intermediate curves. Parameters are chosen as  $\alpha = 0, (h, \tau) = (2^{-7}, 4^{-7})$ .

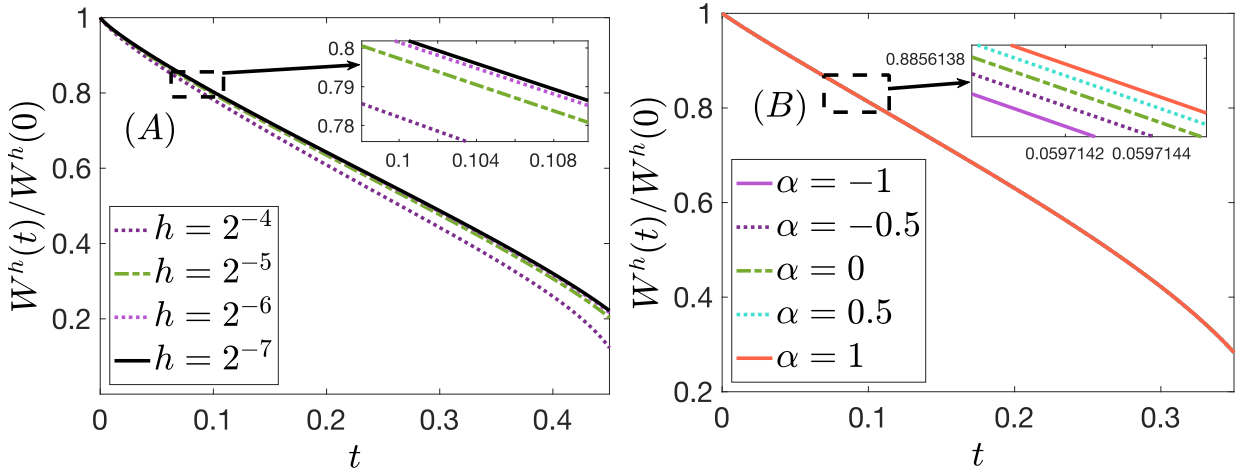


Figure 9: Normalized energy of SP-PFEM (3.7) for (A) Case I with  $\beta = 1/7$  and  $\alpha = 0$ ; and (B) Case II with different values of  $\alpha$ . The mesh sizes for figure (B) are chosen as  $(h, \tau) = (2^{-7}, 4^{-7})$ .

Figure 8–Figure 9 plots the morphological evolution and normalized energy of an ellipse with major axis 4 and minor axis 1 under anisotropic curvature flow by SP-PFEM (3.7). The anisotropy is chosen from the energy density in (A) Case I with  $\beta = 1/7$  and (B) Case II. The observation from Figure 8–Figure 9 reveals that:

- The normalized energy is monotonically decreasing when  $\hat{\gamma}(\theta)$  satisfies the energy stability condition (3.13).
- The energy decay curves of SP-PFEM (3.7) for different values of  $\alpha$  exhibit very similar shapes, indicating robustness of the method with respect to the parameter  $\alpha$ .

### 6.5. Morphological evolution under anisotropic curvature flow

In the following, we employ SP-PFEM (3.7) to simulate the morphological evolution of closed curves governed by anisotropic curvature flow. Unless otherwise specified, the mesh size is set to  $(h, \tau) = (2^{-7}, 4^{-7})$ . We consider the following non-convex initial curve with large variations in the curvature [54]:

$$\begin{cases} x = \cos(2\pi\rho), & \rho \in [0, 1], \\ y = \frac{1}{2} \sin(2\pi\rho) + \sin(\cos(2\pi\rho)) + \sin(2\pi\rho) \left( \frac{1}{5} + \sin(2\pi\rho) \sin^2(6\pi\rho) \right), \end{cases} \quad (6.5)$$

and a  $C^0$ -smooth initial curve with sharp corners and concavities. Results are displayed in Figure 10 and Figure 11, respectively.

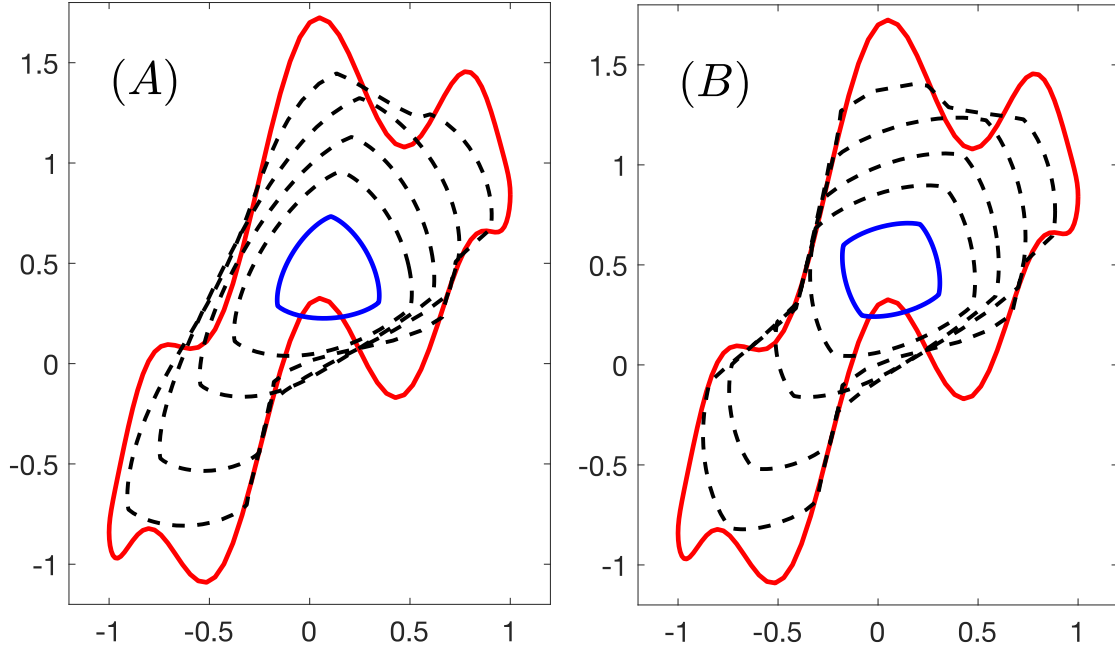


Figure 10: Morphological evolution of a non-convex initial curve with large curvature variations under anisotropic curvature flow by SP-PFEM (3.7) with  $\alpha = 2$ . The red lines represent the initial shapes. The blue lines represent the numerical curves at  $t = 0.32$ . The black dashed lines represent the intermediate curves.

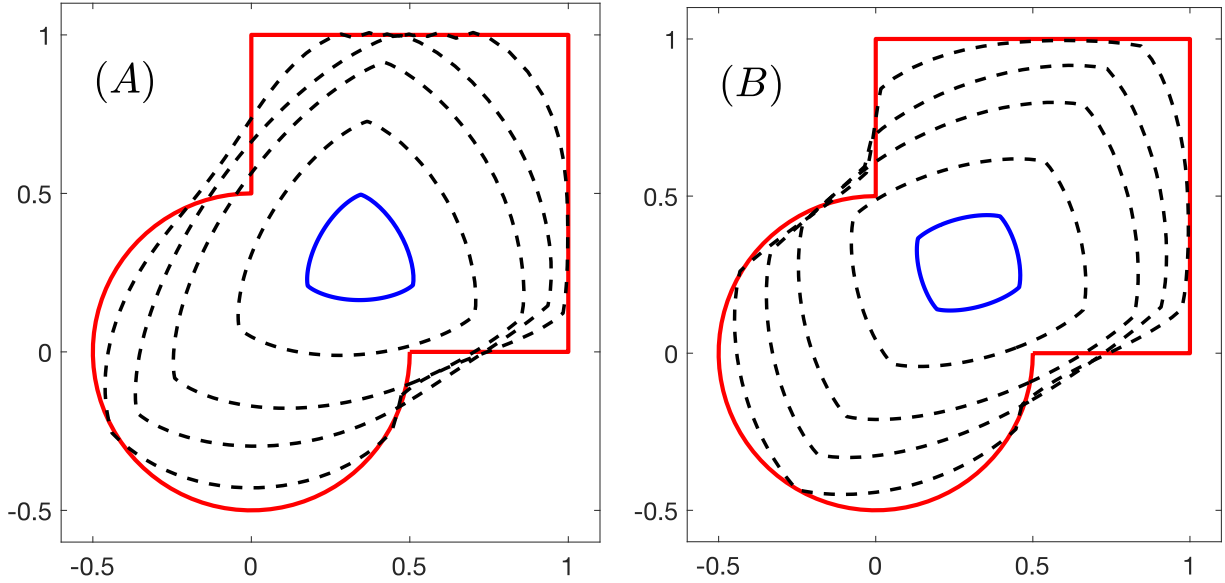


Figure 11: Morphological evolution of an initial curve with  $C^0$ -smoothness under anisotropic curvature flow by SP-PFEM (3.7) with  $\alpha = -2$ . The red lines represent the initial shapes. The blue lines represent the numerical curves at  $t = 0.24$ . The black dashed lines represent the intermediate curves.

In Figure 10–Figure 11, two types of surface energy densities are applied in our simulation: (A)  $\hat{\gamma}(\theta) = 1 + \frac{1}{7} \cos 3\theta$ ; and (B)  $\hat{\gamma}(\theta) = 1 + \frac{1}{12} \cos 4(\theta + \frac{\pi}{6})$ . Observation from Figure 10–Figure 11 reveals that, under the anisotropic curvature flow, the curve will gradually shrink, while its shape tends to evolve toward a common form determined by the same anisotropy.

*Evolution of a self-intersecting curve*

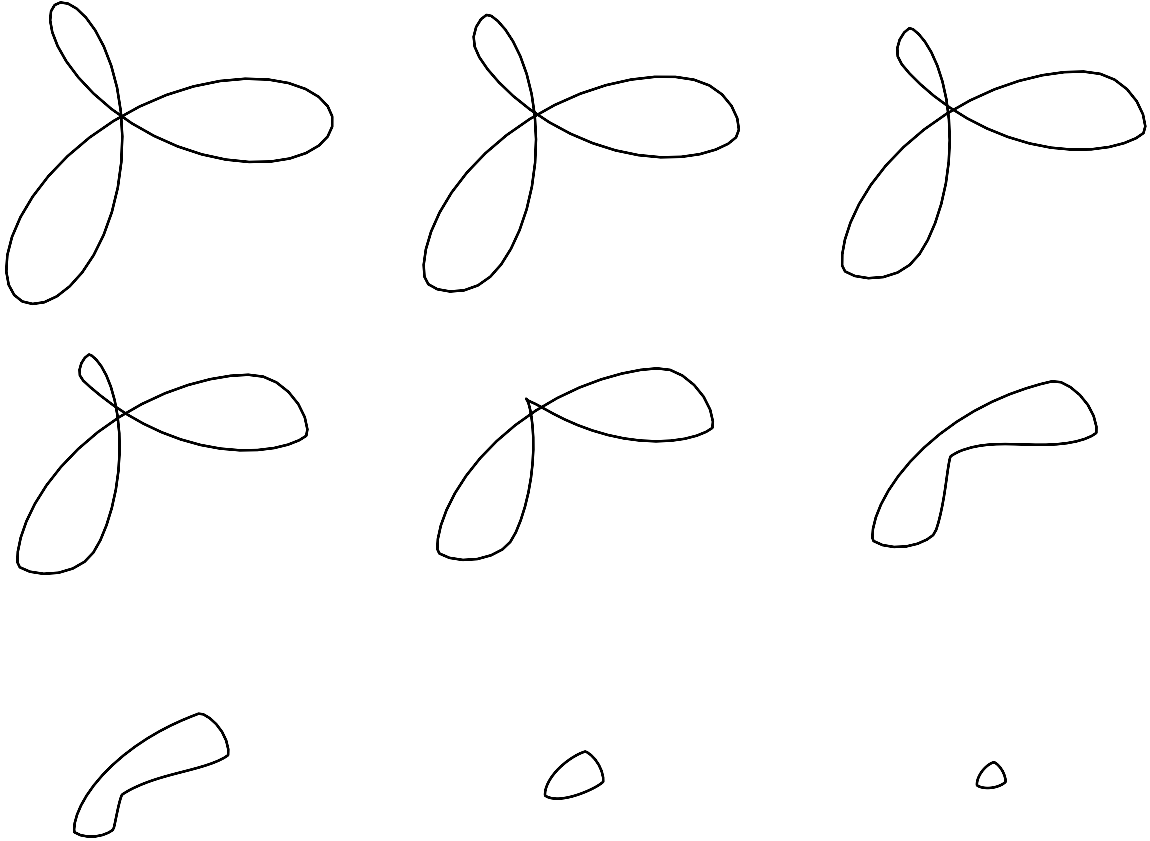


Figure 12: Plots of the anisotropic evolution of a self-intersecting initial curve at times  $t = 0, 0.028, 0.056, 0.084, 0.112, 0.2, 0.3, 0.4, 0.42$ . A 3-fold anisotropy  $\hat{\gamma}(\theta) = 1 + \frac{1}{9} \cos 3\theta$  is used for the surface energy density. Other parameters are set as  $\alpha = -1, h = 2^{-7}, \tau = 0.005$ .

As is theoretically known, self-intersecting curves often develop singularities during curvature-driven evolution. The local geometry around these points becomes highly complex, posing significant challenges for numerical simulation. Figure 12 illustrates the anisotropic evolution of an initial curve with a triple self-intersection point. A similar example was presented in [29, Fig 7.2] for the isotropic case. The numerical results demonstrate that our method remains effective in capturing cusp singularities even in the presence of anisotropy.

*6.6. Numerical results for other anisotropic flows*

In this part, we present numerical experiments for two types of anisotropic flows that preserve area: the area-conserved anisotropic curvature flow and anisotropic surface diffusion. The following normalized area loss is introduced as an indicator to numerically demonstrate the area conservation property [62]:

$$\frac{\Delta A^h(t)}{A^h(0)} \Big|_{t=t_m} := \frac{A^{m+1} - A^0}{A^0}, \quad \forall m \geq 0. \quad (6.6)$$

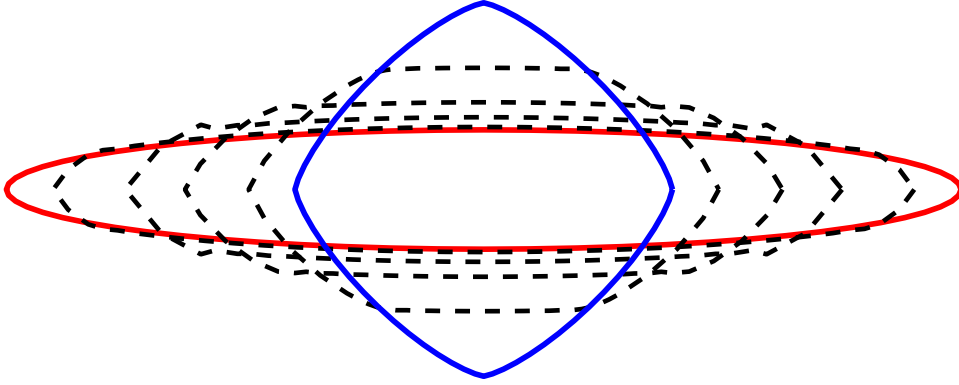


Figure 13: Morphological evolution of an ellipse with major axis 8 and minor axis 1 under area-conserved anisotropic curvature flow by SP-PFEM (5.3) with the  $l^4$ -norm metric anisotropy  $\hat{\gamma}(\theta) = \sqrt[4]{n_1^4 + n_2^4}$ , where  $\mathbf{n} = (n_1, n_2)^T = (-\sin \theta, \cos \theta)^T$ . The red and blue lines represent the initial shape and the numerical equilibrium, respectively; and the black dash lines represent the intermediate curves. Parameters are set to  $\alpha = 2.5$ ,  $(h, \tau) = (2^{-6}, 4^{-6})$ .

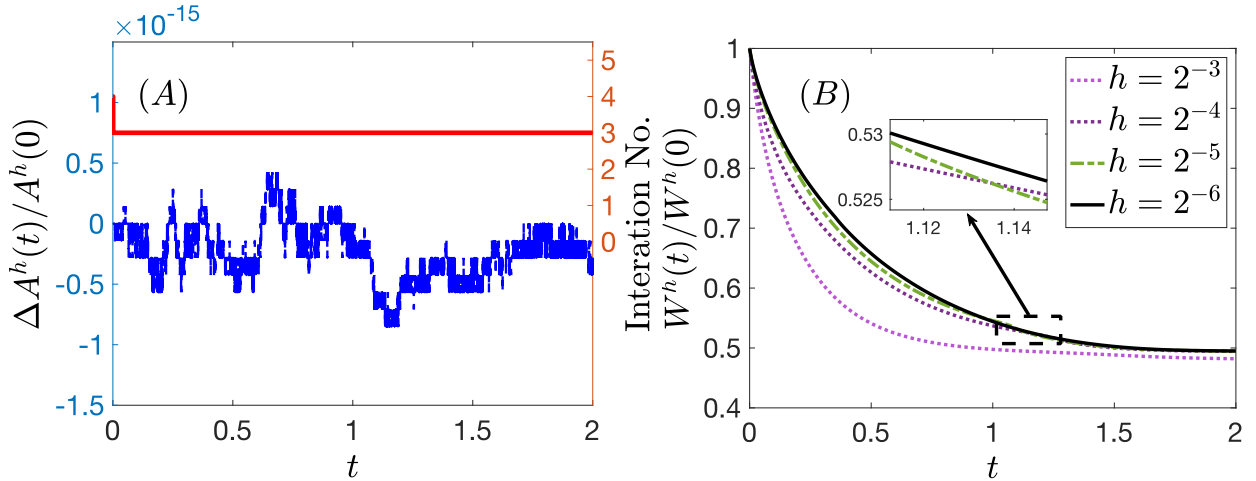


Figure 14: Temporal evolution of (A) normalized area loss (blue dash line) and iteration number (red line); and (B) normalized energy of SP-PFEM (5.3) for the anisotropic curvature flow in Figure 13.

### 6.6.1. Area-conserved anisotropic curvature flow

Figure 13 illustrates the morphological evolution of an ellipse with major axis 8 and minor axis 1 under the area-conserved anisotropic curvature flow. The surface energy density is the so-called  $l^4$ -norm metric anisotropy:  $\hat{\gamma}(\theta) = \sqrt[4]{n_1^4 + n_2^4}$ , where  $\mathbf{n} = (n_1, n_2)^T = (-\sin \theta, \cos \theta)^T$  [3]. The normalized area loss and the number of Newton's iteration are plotted in Figure 14 (A). The normalized area loss is observed to be on the order of  $10^{-15}$ , which is very close to rounding error. This indicates that the area is conserved in the sense of machine precision. The number of Newton iterations quickly decreases from 4 at the beginning to 3. And the normalized energy is monotonically decreasing, as shown in Figure 14 (B).

We also apply SP-PFEM (5.3) to simulate the morphological evolution of some complex initial curves governed by area-conserved anisotropic curvature flow. The results are shown in Figure 15–Figure 16. Two types of curves are considered as follows:

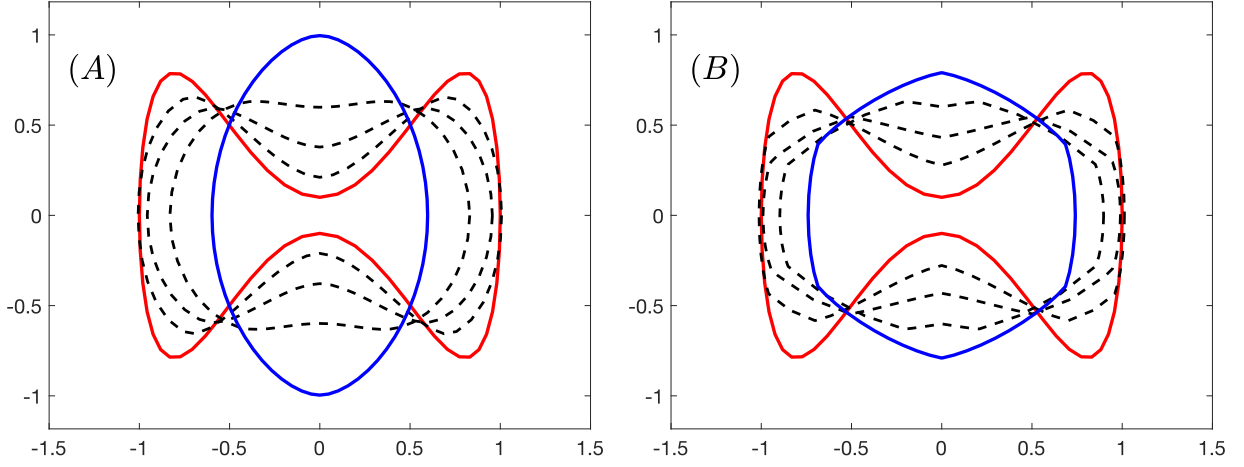


Figure 15: Morphological evolution of a bowtie-shaped curve under area-conserved anisotropic curvature flow with anisotropy (A)  $\hat{\gamma}(\theta) = 1 + \frac{1}{28} \cos 2\theta$ ; and (B)  $\hat{\gamma}(\theta) = 1 + \frac{1}{30} \cos 6\theta$ . The red and blue lines represent the initial shape and the numerical equilibrium, respectively; and the black dash lines represent the intermediate curves. Other parameter are set as  $\alpha = 0.5, (h, \tau) = (2^{-6}, 4^{-6})$ .

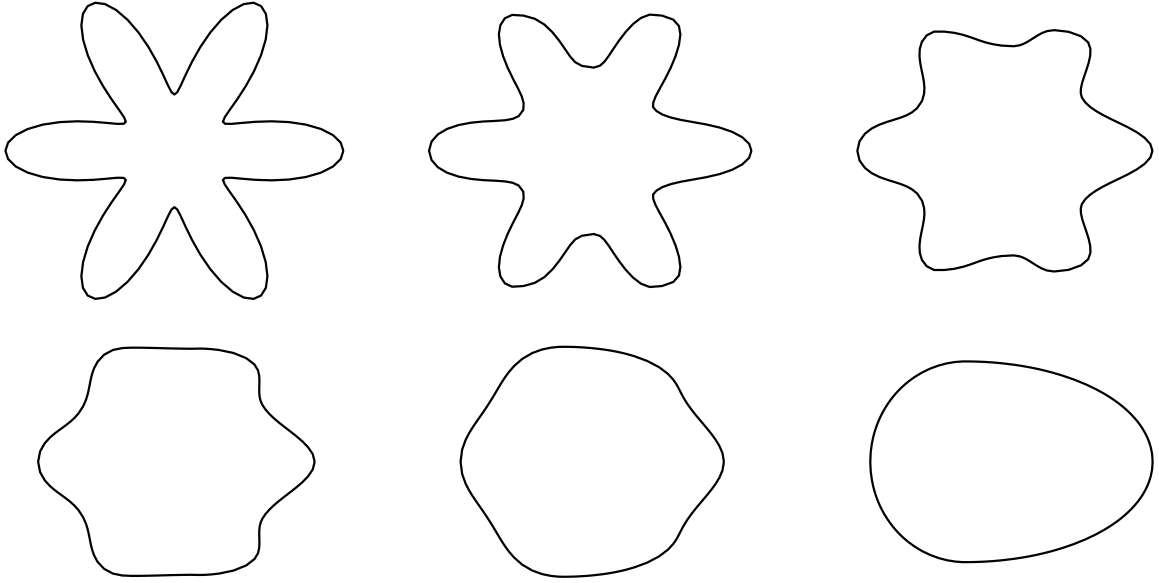


Figure 16: Snapshots of a flower initial curve under area-conserved anisotropic curvature flow with anisotropy Case II at times  $t = 0, 0.05, 0.15, 0.25, 0.4, 2.5$ . Other parameter are set as  $\alpha = -0.5, h = 2^{-7}, \tau = 0.005$ .

- a bowtie-shaped curve:

$$\begin{cases} x = \cos(2\pi\rho), \\ y = 2 \sin(2\pi\rho) - 1.9 \sin^3(2\pi\rho), \end{cases} \quad \rho \in [0, 1]; \quad (6.7)$$

- a flower-shaped curve:

$$\begin{cases} x = (2 + \cos(12\pi\rho)) \cos(2\pi\rho), \\ y = (2 + \cos(12\pi\rho)) \sin(2\pi\rho), \end{cases} \quad \rho \in [0, 1]. \quad (6.8)$$

It can be observed that, as theoretically predicted, both curves gradually evolve toward the Wulff shape corresponding to the given anisotropy [60].

### 6.6.2. Anisotropic surface diffusion

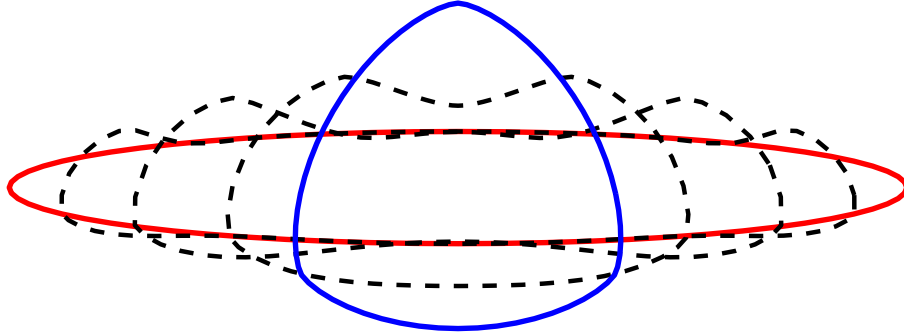


Figure 17: Morphological evolution of an ellipse with major axis 8 and minor axis 1 governed by anisotropic surface diffusion for Case I with  $\beta = 1/9$ . The red and blue lines represent the initial shape and the numerical equilibrium, respectively; and the black dash lines represent the intermediate curves. Mesh sizes are set to  $(h, \tau) = (2^{-6}, 4^{-6})$ .

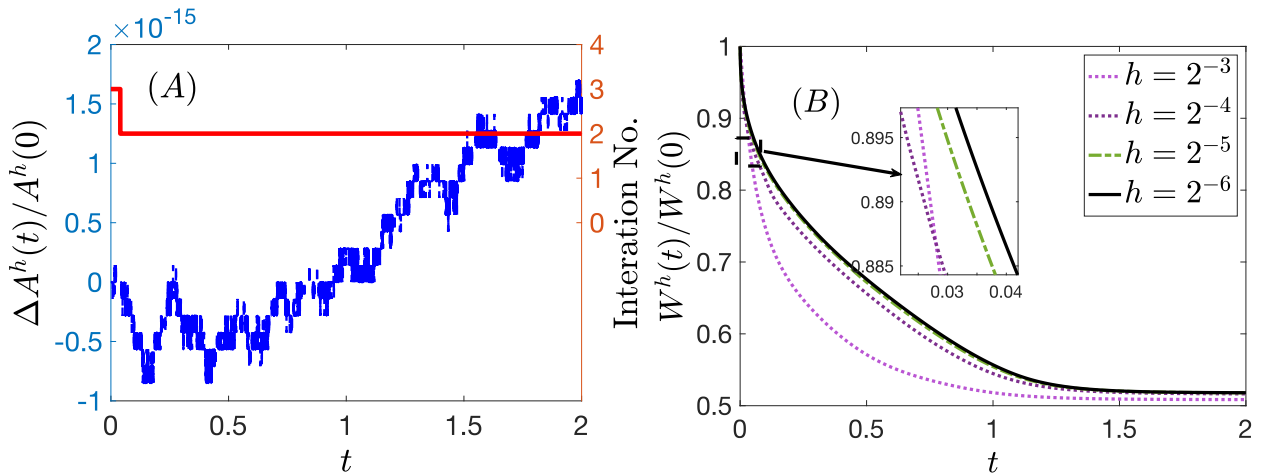


Figure 18: Temporal evolution of (A) normalized area loss (blue dash line) and iteration number (red line); and (B) normalized energy of SP-PFEM (5.6) for the anisotropic surface diffusion in Figure 17.

Figure 17–Figure 18 illustrate the evolution of an 8:1 ellipse under anisotropic surface diffusion, along with the corresponding changes in the normalized area, the iteration number and the normalized energy. The surface energy density is chosen as in Case I with  $\beta = 1/9$ . Results in Figure 18 confirm that our method is numerically area conservative and energy dissipative when condition (3.13) is satisfied.

Figure 19 presents numerical experiments on a quadrifolium. Escher et al. [33] and Barrett et al. [11] have previously simulated the evolution of the quadrifolium under isotropic surface diffusion, demonstrating that the limiting curve is a triply covered circle. Our results show that the behavior under anisotropic surface diffusion is qualitatively similar: for positive time, the winding number of the curve with respect to the origin remains unchanged, and the limiting shape becomes a triply covered Wulff shape corresponding to the given anisotropy (cf. Figure 19).

The initial curve in Figure 20 is given by a  $2 \times 2$  square minus a thin rectangle ( $0.02 \times 1.8$ ). The shape was described by Bänsch [2] as an *almost slit domain*. Previous studies [2, 11] have been shown

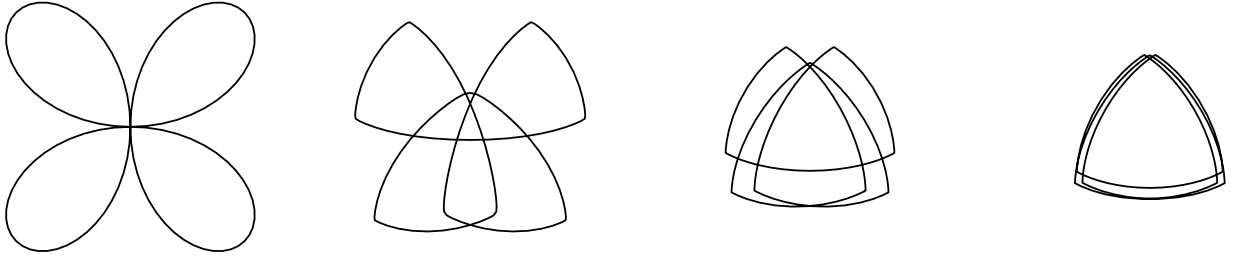


Figure 19: Anisotropic surface diffusion of a quadrifolium with anisotropy Case I at times  $t = 0, 0.15, 0.5, 0.9$ . Parameters are set as  $\alpha = 0.5, \beta = 1/5, h = 2^{-7}, \tau = 0.001$ .

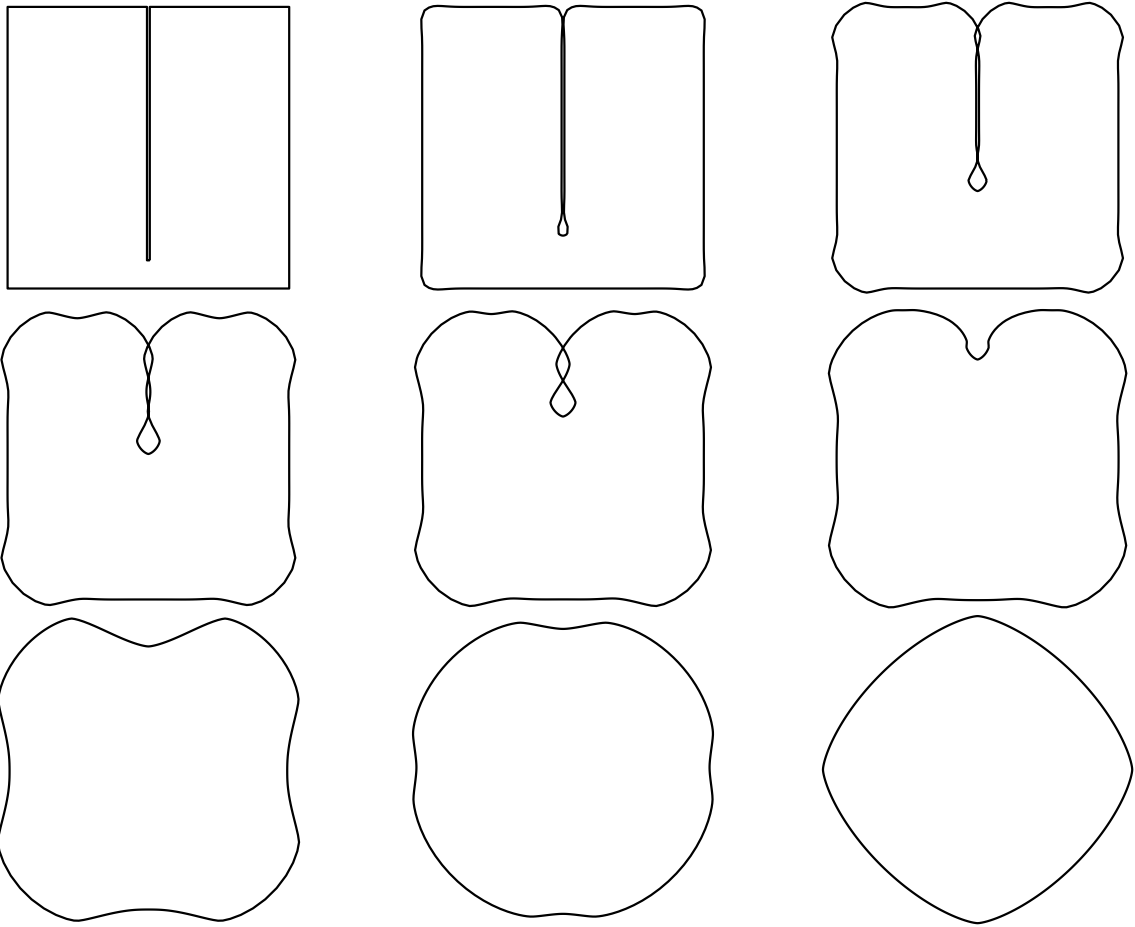


Figure 20: Anisotropic surface diffusion of an almost slit domain with 4-fold anisotropy  $\hat{\gamma}(\theta) = 1 + \frac{1}{16} \cos 4\theta$  at times  $t = 0, 5 \times 10^{-6}, 7 \times 10^{-5}, 2.5 \times 10^{-4}, 5 \times 10^{-4}, 7.5 \times 10^{-4}, 0.002, 0.02, 0.1$ . Parameters are set as  $a = 1, h = 1/288, \tau = 1 \times 10^{-6}$ .

that this curve undergoes a pinch-off phenomenon under isotropic surface diffusion due to a curve crossing. Our numerical simulations reveal that such behavior persists under anisotropic surface diffusion as well. Notably, compared to the methods of [2, 11], our approach guarantees exact area conservation during the entire evolution process.

We also conducted experiments on the lemniscate of Bernoulli, the results can be found in Figure 21. As is known, the signed area enclosed by the Bernoulli's lemniscate is identically zero. Since anisotropic surface diffusion decreases the total energy (i.e. the weighted perimeter) while preserving area, it is reasonable to

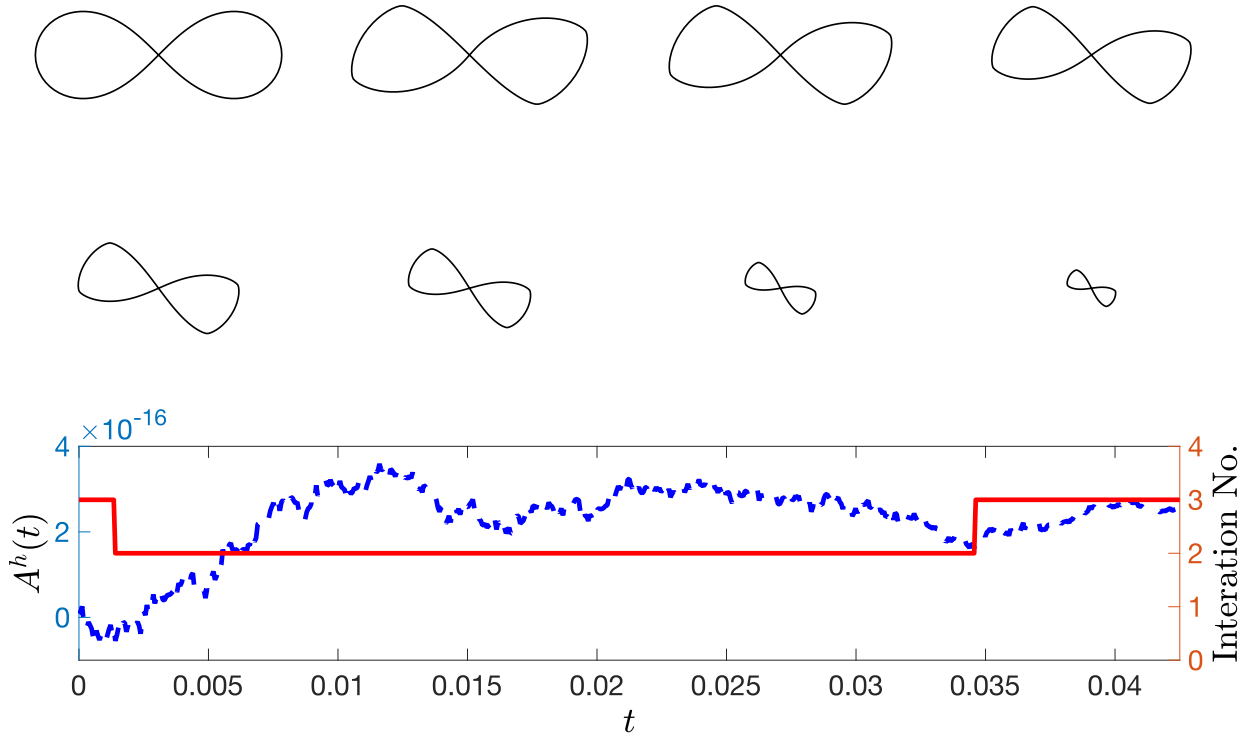


Figure 21: Evolution of the Bernoulli's lemniscate governed by anisotropic surface diffusion with anisotropy Case I at times  $t = 0, 0.008, 0.015, 0.025, 0.035, 0.04, 0.0425$ . Parameters are chosen as  $\beta = 1/9, (h, \tau) = (2^{-7}, 4^{-7})$ .

expect the curve to shrink to a point. Our numerical experiments support this conjecture: the observed enclosed area remains at the order of  $10^{-16}$  throughout the simulation, effectively zero within machine precision. Meanwhile, each lobe of the curve gradually approaches the corresponding Wulff shape before ultimately collapsing into a single point. Interestingly, the entire curve exhibits a slow rotational motion during the evolution due to the anisotropic effects. Such a phenomenon does not occur in the isotropic setting, where the curve shrinks in place without changing orientation as shown in [33].

### 6.7. Evolution of long thin films under anisotropic surface diffusion

The morphological evolution of crystal-grown thin films under anisotropic surface diffusion has attracted significant attention in materials science and solid-state physics [57], with profound applications in heterogeneous catalysis [51], quantum dot manufacturing [35] and solid-state dewetting [59]. According to studies [24, 41], once the island aspect ratio exceeds a certain critical threshold, the structure becomes unstable and undergoes pinch-off, resulting in the formation of multiple separate islands. In this section, we apply the SP-PFEM (5.6) to simulate the pinch-off phenomenon of long thin films under anisotropic surface diffusion.

First, we perform simulations of the evolution of a long thin film with an aspect ratio of 50 under 4-fold anisotropy  $\hat{\gamma}(\theta) = 1 + \frac{1}{16} \cos 4\theta$ . Figure 22 illustrates the evolution of the normalized area and the normalized energy. In this case, the pinch-off occurs at  $t = 140.5$ . It can be observed that, when the pinch-off happens, the energy exhibits a sharp drop while the area remains conserved.

In addition to the aspect ratio of the thin film, the anisotropy strength of the surface energy also plays a crucial role in the island formation process. We conducted experiments with varying aspect ratios and anisotropy strengths to investigate their influence on the formation of islands. The results are presented in Figure 23-Figure 24 for commonly used  $m$ -fold anisotropies  $\hat{\gamma}(\theta) = 1 + \beta \cos m\theta$ ,  $m = 2, 3, 4, 6$ .

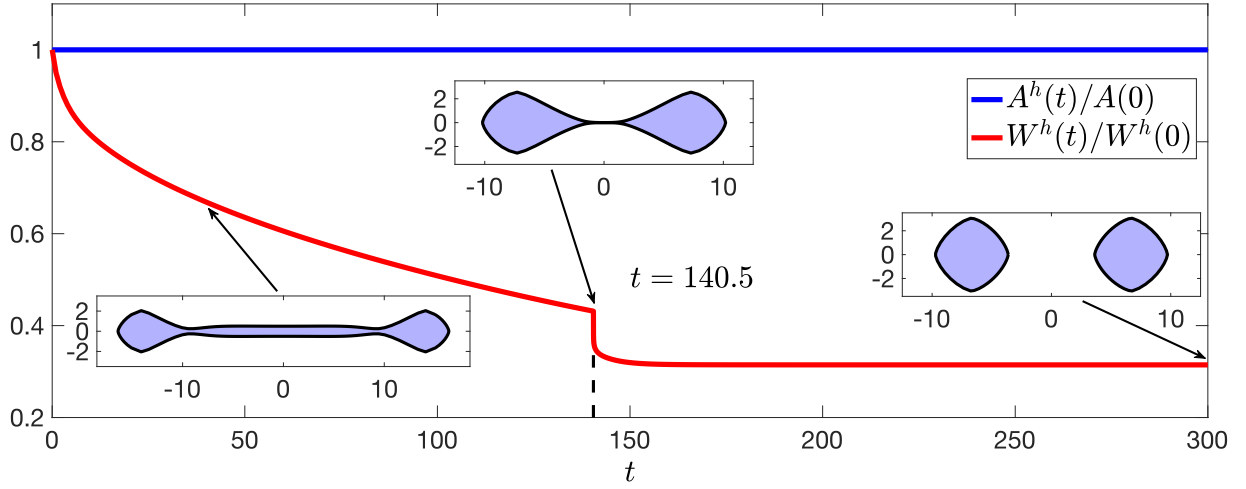


Figure 22: Normalized area and energy of a long thin film (aspect ratio of 50) governed by anisotropic surface diffusion with the 4-fold anisotropy  $\hat{\gamma}(\theta) = 1 + \frac{1}{16} \cos 4\theta$ .

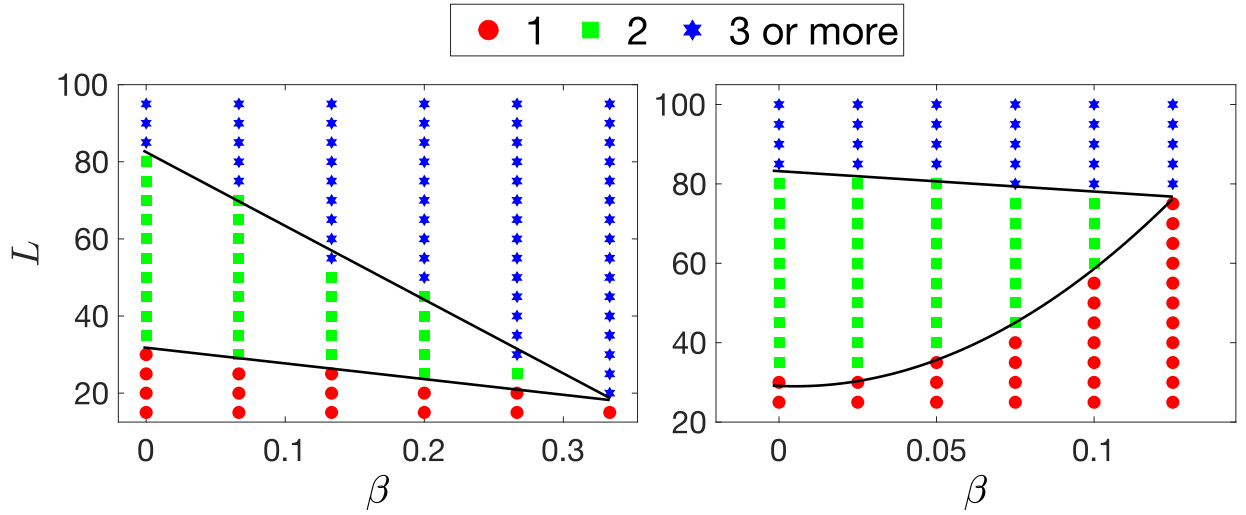


Figure 23: The number of islands formed from the pinch-off of a  $2L \times 1$  long thin film as a function of  $L$  and anisotropy strength  $\beta$  for: (left) the 2-fold anisotropy  $\hat{\gamma}(\theta) = 1 + \beta \cos 2\theta$ ; (right) the 3-fold anisotropy  $\hat{\gamma}(\theta) = 1 + \beta \cos 4\theta$ . The solid lines represent the 1-2 islands and 2-3 islands boundaries.

For the symmetric anisotropy  $\hat{\gamma}(\theta) = 1 + \beta \cos m\theta$ ,  $m = 2, 4, 6$ , the boundaries between the 1-2 islands and 2-3 islands regions are approximated by the following linear curve fitting  $L = p(m)\beta + q(m)$ :

- 1-2 islands boundary:  $p(m) = -12.23m^2 + 8.04m - 7.86, q(m) = 0.36m + 31.31$ ;
- 2-3 islands boundary:  $p(m) = -35.07m^2 - 165.40m + 279.82, q(m) = 0.18m + 83.06$ .

Numerical results indicate that, for a given aspect ratio, increasing the anisotropy strength of symmetric surface energy promotes the formation of more islands.

For the asymmetric anisotropy  $\hat{\gamma}(\theta) = 1 + \beta \cos 3\theta$ , we use a quadratic curve fitting  $L = 3285.70\beta^2 - 33.57\beta + 29.11$  to determine the boundary between the 1-2 islands regions, and a linear curve fitting  $L = -51.43\beta + 83.21$  to identify the 2-3 islands boundary. Our numerical results show that, for smaller aspect

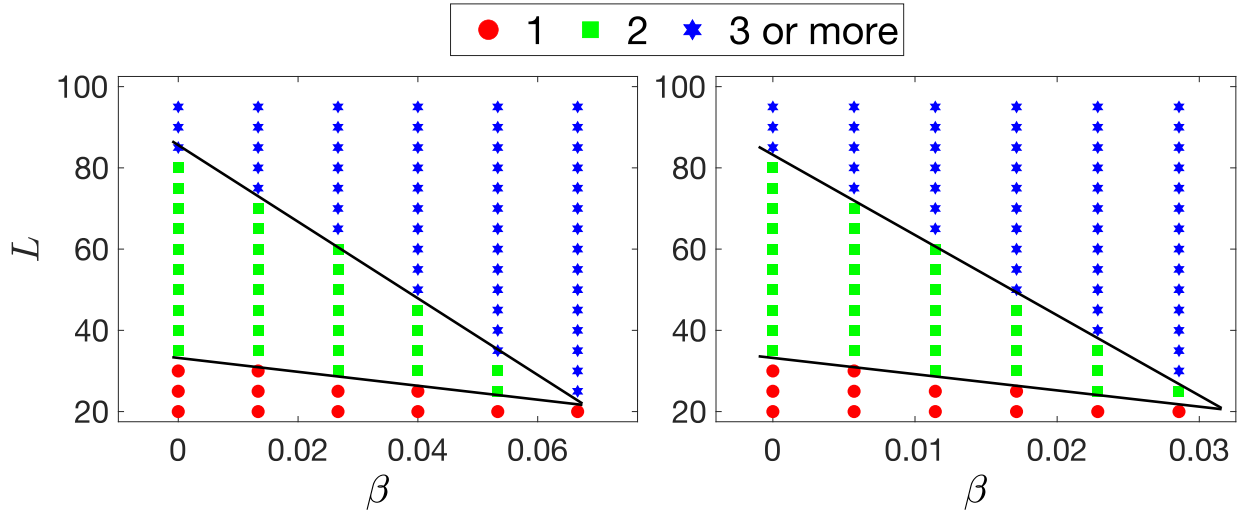


Figure 24: The number of islands formed from the pinch-off of a  $2L \times 1$  long thin film as a function of  $L$  and anisotropy strength  $\beta$  for: (left) the 4-fold anisotropy  $\hat{\gamma}(\theta) = 1 + \beta \cos 4\theta$ ; (right) the 6-fold anisotropy  $\hat{\gamma}(\theta) = 1 + \beta \cos 6\theta$ . The solid lines represent the 1-2 islands and 2-3 islands boundaries.

ratios, increasing the anisotropy strength tends to produce fewer islands. This behavior is attributed to the asymmetry in surface energy. A comparison of the two sets of simulation results reveals that, for the evolution of long thin films, symmetric and asymmetric anisotropies may lead to markedly different morphological behaviors.

## 7. Conclusion

We provided a detailed analysis and comparison of the structure-preserving parametric finite element methods (SP-PFEM) for anisotropic geometric flows. By introducing a hyperparameter  $\alpha$ , we are able to express all possible surface energy matrices in a unified form, thereby incorporating the SP-PFEM schemes into a single analytical framework. It is proven that  $3\hat{\gamma}(\theta) - \hat{\gamma}(\theta - \pi) > 0$  serves as a common energy stability condition for all surface energy matrices. In the special case where the surface energy matrix is symmetric, this condition can be improved to  $3\hat{\gamma}(\theta) - \hat{\gamma}(\theta - \pi) \geq 0$ , which is both necessary and sufficient for the energy stability. Apart from mesh quality, the proposed method exhibits consistent performance across different values of  $\alpha$  in terms of accuracy, computational efficiency, and structure preservation, indicating a certain degree of robustness. The method presented in this paper can be easily extended to general anisotropic geometric flows, including area-conserved anisotropic curvature flow and anisotropic surface diffusion. It provides an effective framework for developing structure-preserving numerical algorithms for general anisotropic curvature-driven problems.

## Acknowledgement

This work was partially supported by the Ministry of Education of Singapore under its AcRF Tier 1 funding A-8003584-00-00 (W. Bao), the Alexander von Humboldt Foundation (Y. Li), the National Natural Science Foundation of China in the Division of Mathematical Sciences Project No. 12471342 (W. Ying) and Zhiyuan Honors Program for Graduate Students in Shanghai Jiao Tong University (Y. Zhang).

## References

- [1] L. Alvarez, F. Guichard, P.-L. Lions and J.-M. Morel, *Axioms and fundamental equations of image processing*, Arch. Ration. Mech. Anal., 123 (1993), pp. 199– 257.
- [2] E. Bänsch, P. Morin and R. Nochetto, *A finite element method for surface diffusion: the parametric case*, J. Comput. Phys., 203(1) (2005), pp. 321– 343.
- [3] W. Bao, W. Jiang and Y. Li, *A symmetrized parametric finite element method for anisotropic surface diffusion of closed curves*, SIAM J. Numer. Anal., 61(2) (2023), pp. 617– 641.
- [4] W. Bao and Y. Li, *A structure-preserving parametric finite element method for geometric flows with anisotropic surface energy*, Numer. Math., 156 (2024), pp. 609– 639.
- [5] W. Bao and Y. Li, *A unified structure-preserving parametric finite element method for anisotropic surface diffusion*, Math. Comp., 94(355) (2025), pp. 2113– 2149.
- [6] W. Bao, Y. Li and Q. Zhao, *A structure-preserving parametric finite element method for solid-state dewetting on curved substrates*, Commun. Nonlinear Sci. Numer. Simul. (2025), pp. 108767.
- [7] W. Bao and Q. Zhao, *A structure-preserving parametric finite element method for surface diffusion*, SIAM J. Numer. Anal., 59(5) (2021), pp. 2775– 2799.
- [8] W. Bao and Q. Zhao, *An energy-stable parametric finite element method for simulating solid-state dewetting problems in three dimensions*, J. Comput. Math., 41(4) (2023), pp. 771– 796.
- [9] W. Bao, W. Jiang, Y. Wang and Q. Zhao, *A parametric finite element method for solid-state dewetting problems with anisotropic surface energies*, J. Comput. Phys., 330 (2017), pp. 380– 400.
- [10] W. Bao, H. Garcke, R. Nürnberg and Q. Zhao, *Volume-preserving parametric finite element methods for axisymmetric geometric evolution equations*, J. Comput. Phys., 460 (2022), pp. 111180.
- [11] J. Barrett, H. Garcke and R. Nürnberg, *A parametric finite element method for fourth order geometric evolution equations*, J. Comput. Phys., 222(1) (2007), pp. 441– 467.
- [12] J. Barrett, H. Garcke and R. Nürnberg, *On the variational approximation of combined second and fourth order geometric evolution equations*, SIAM J. Sci. Comput., 29(3) (2007), pp. 1006– 1041.
- [13] J. Barrett, H. Garcke and R. Nürnberg, *A variational formulation of anisotropic geometric evolution equations in higher dimensions*, Numer. Math., 109(1) (2008), pp. 1– 44.
- [14] J. Barrett, H. Garcke and R. Nürnberg, *Numerical approximation of anisotropic geometric evolution equations in the plane*, IMA J. Numer. Anal., 28(2) (2008), pp. 292– 330.
- [15] J. Barrett, H. Garcke and R. Nürnberg, *On the parametric finite element approximation of evolving hypersurfaces in  $R^3$* , J. Comput. Phys., 227(9) (2008), pp. 4281– 4307.
- [16] J. Barrett, H. Garcke and R. Nürnberg, *On stable parametric finite element methods for the Stefan problem and the Mullins–Sekerka problem with applications to dendritic growth*, J. Comput. Phys., 229(18) (2010), pp. 6270– 6299.
- [17] J. Barrett, H. Garcke and R. Nürnberg, *Parametric approximation of surface clusters driven by isotropic and anisotropic surface energies*, Interfaces Free Bound., 12(2) (2010), pp. 187– 234.
- [18] J. Barrett, H. Garcke and R. Nürnberg, *Parametric finite element approximations of curvature-driven interface evolutions*, , 21 (2020), pp. 275– 423.
- [19] M. Brassel and E. Bretin, *A modified phase field approximation for mean curvature flow with conservation of the volume*, Math. Methods Appl. Sci., 34(10) (2011), pp. 1157– 1180.

- [20] M. Burger, F. Haußer, C. Stöcker and A. Voigt, *A level set approach to anisotropic flows with curvature regularization*, J. Comput. Phys., 225(1) (2007), pp. 183– 205.
- [21] U. Clarenz, U. Diewald and M. Rumpf, *Anisotropic geometric diffusion in surface processing*, (2000).
- [22] K. Deckelnick, G. Dziuk and C. Elliott, *Computation of geometric partial differential equations and mean curvature flow*, Acta Numer., 14 (2005), pp. 139– 232.
- [23] K. Deckelnick, G. Dziuk and C. Elliott, *Fully discrete finite element approximation for anisotropic surface diffusion of graphs*, SIAM J. Numer. Anal., 43(3) (2005), pp. 1112– 1138.
- [24] E. Dornel, J.-C. Barbe, F. De Crécy, G. Lacolle and J. Eymery, *Surface diffusion dewetting of thin solid films: Numerical method and application to Si/ SiO<sub>2</sub>*, Phys. Rev. B, 73(11) (2006), pp. 115427.
- [25] P. Du, M. Khenner and H. Wong, *A tangent-plane marker-particle method for the computation of three-dimensional solid surfaces evolving by surface diffusion on a substrate*, J. Comput. Phys., 229(3) (2010), pp. 813– 827.
- [26] Q. Du and X. Feng, *The phase field method for geometric moving interfaces and their numerical approximations*, Handbook of numerical analysis, 21 (2020), pp. 425– 508.
- [27] G. Dziuk, *An algorithm for evolutionary surfaces*, Numer. Math., 58(1) (1990), pp. 603– 611.
- [28] G. Dziuk, *Convergence of a semi-discrete scheme for the curve shortening flow*, Math. Models Methods Appl. Sci., 4(04) (1994), pp. 589– 606.
- [29] G. Dziuk, *Discrete anisotropic curve shortening flow*, SIAM J. Numer. Anal., 36(6) (1999), pp. 1808– 1830.
- [30] T. Einstein, *Equilibrium shape of crystals*, (2015), pp. 215– 264.
- [31] C. Elliott and H. Garcke, *Diffusional phase transitions in multicomponent systems with a concentration dependent mobility matrix*, Physica D, 109(3-4) (1997), pp. 242– 256.
- [32] J. Escher, Y. Giga and K. Ito, *On a limiting motion and self-intersections of curves moved by the intermediate surface diffusion flow*, Nonlinear Anal., 47(6) (2001), pp. 3717– 3728.
- [33] J. Escher, U. Mayer and G. Simonett, *The surface diffusion flow for immersed hypersurfaces*, SIAM J. Math. Anal., 29(6) (1998), pp. 1419– 1433.
- [34] T. Eto, H. Garcke and R. Nürnberg, *A parametric finite element method for a degenerate multi-phase Stefan problem with triple junctions*, arXiv preprint arXiv:2505.13165 (2025).
- [35] I. Fonseca, A. Pratelli and B. Zwicknagl, *Shapes of epitaxially grown quantum dots*, Arch. Ration. Mech. Anal., 214 (2014), pp. 359– 401.
- [36] H. Garcke, R. Nürnberg and Q. Zhao, *Structure-preserving discretizations of two-phase Navier–Stokes flow using fitted and unfitted approaches*, J. Comput. Phys., 489 (2023), pp. 112276.
- [37] H. Garcke, R. Nürnberg and Q. Zhao, *A variational front-tracking method for multiphase flow with triple junctions*, Math. Comp. (2025).
- [38] M. Gurtin and M. Jabbour, *Interface Evolution in Three Dimensions with Curvature-Dependent Energy and Surface Diffusion: Interface-Controlled Evolution, Phase Transitions, Epitaxial Growth of Elastic Films*, Arch. Ration. Mech. Anal., 163 (2002), pp. 171– 208.
- [39] J. Hu and B. Li, *Evolving finite element methods with an artificial tangential velocity for mean curvature flow and Willmore flow*, Numer. Math., 152(1) (2022), pp. 127– 181.

- [40] W. Jiang and Q. Zhao, *Sharp-interface approach for simulating solid-state dewetting in two dimensions: A Cahn–Hoffman  $\xi$ -vector formulation*, *Physica D*, 390 (2019), pp. 69– 83.
- [41] W. Jiang, W. Bao, C. Thompson and D. Srolovitz, *Phase field approach for simulating solid-state dewetting problems*, *Acta Mater.*, 60(15) (2012), pp. 5578– 5592.
- [42] W. Jiang, Y. Wang, Q. Zhao, D. Srolovitz and W. Bao, *Solid-state dewetting and island morphologies in strongly anisotropic materials*, *Scripta Mater.*, 115 (2016), pp. 123– 127.
- [43] W. Jiang, Y. Wang, D. Srolovitz and W. Bao, *Solid-state dewetting on curved substrates*, *Phys. Rev. Materials*, 2(11) (2018), pp. 113401.
- [44] B. Kovács, B. Li and C. Lubich, *A convergent evolving finite element algorithm for mean curvature flow of closed surfaces*, *Numer. Math.*, 143 (2019), pp. 797– 853.
- [45] B. Kovács, B. Li and C. Lubich, *A convergent evolving finite element algorithm for Willmore flow of closed surfaces*, *Numer. Math.*, 149(3) (2021), pp. 595– 643.
- [46] Y. Li and W. Bao, *An energy-stable parametric finite element method for anisotropic surface diffusion*, *J. Comput. Phys.*, 446 (2021), pp. 110658.
- [47] Y. Li, W. Ying and Y. Zhang, *A structure-preserving parametric finite element method with optimal energy stability condition for anisotropic surface diffusion*, *J. Sci. Comput.*, 104(3) (2025), pp. 76.
- [48] A. Maxwell, C. Thompson and W. Carter, *A level-set method for simulating solid-state dewetting in systems with strong crystalline anisotropy*, *Acta Mater.*, 282 (2025), pp. 120368.
- [49] S. Osher and R. Fedkiw, *Level set methods: an overview and some recent results*, *J. Comput. Phys.*, 169(2) (2001), pp. 463– 502.
- [50] B. Palmer, *Stability of the Wulff shape*, *Proc. Amer. Math. Soc.*, 126(12) (1998), pp. 3661– 3667.
- [51] S. Randolph, J. Fowlkes, A. Melechko, K. Klein, H. Meyer, M. Simpson and P. Rack, *Controlling thin film structure for the dewetting of catalyst nanoparticle arrays for subsequent carbon nanofiber growth*, *Nanotechnology*, 18(46) (2007), pp. 465304.
- [52] O. Reynolds, *Papers on mechanical and physical subjects*, (1983).
- [53] G. Sapiro and A. Tannenbaum, *On affine plane curve evolution*, *J. Funct. Anal.*, 119(1) (1994), pp. 79– 120.
- [54] D. Sevcovic and K. Mikula, *Evolution of plane curves driven by a nonlinear function of curvature and anisotropy*, *SIAM J. Appl. Math.*, 61(5) (2001), pp. 1473– 1501.
- [55] J. Taylor, *II—mean curvature and weighted mean curvature*, *Acta Metall. Mater.*, 40(7) (1992), pp. 1475– 1485.
- [56] J. Taylor and J. Cahn, *Linking anisotropic sharp and diffuse surface motion laws via gradient flows*, *J. Statist. Phys.*, 77 (1994), pp. 183– 197.
- [57] C. Thompson, *Solid-state dewetting of thin films*, *Annu. Rev. Mater. Res.*, 42 (2012), pp. 399– 434.
- [58] Y. Wang, *Modeling and simulation for solid-state dewetting problems in two dimensions*, National University of Singapore (2016).
- [59] L. Xue and Y. Han, *Pattern formation by dewetting of polymer thin film*, *Progr. Polymer Sci.*, 36(2) (2011), pp. 269– 293.

- [60] S. Yazaki, *On an area-preserving crystalline motion*, Calc. Var. Partial Differential Equations, 14 (2002), pp. 85– 105.
- [61] J. Ye and C. Thompson, *Mechanisms of complex morphological evolution during solid-state dewetting of single-crystal nickel thin films*, Appl. Phys. Lett., 97(7) (2010).
- [62] Y. Zhang, Y. Li and W. Ying, *A stabilized parametric finite element method for surface diffusion with an arbitrary surface energy*, J. Comput. Phys., 523 (2025), pp. 113605.
- [63] Q. Zhao, W. Jiang and W. Bao, *An energy-stable parametric finite element method for simulating solid-state dewetting*, IMA J. Numer. Anal., 41(3) (2021), pp. 2026– 2055.